



LAWRENCE
LIVERMORE
NATIONAL
LABORATORY

FY10 LLNL OMEGA Experimental Programs

R. Tommasini

October 1, 2010

Disclaimer

This document was prepared as an account of work sponsored by an agency of the United States government. Neither the United States government nor Lawrence Livermore National Security, LLC, nor any of their employees makes any warranty, expressed or implied, or assumes any legal liability or responsibility for the accuracy, completeness, or usefulness of any information, apparatus, product, or process disclosed, or represents that its use would not infringe privately owned rights. Reference herein to any specific commercial product, process, or service by trade name, trademark, manufacturer, or otherwise does not necessarily constitute or imply its endorsement, recommendation, or favoring by the United States government or Lawrence Livermore National Security, LLC. The views and opinions of authors expressed herein do not necessarily state or reflect those of the United States government or Lawrence Livermore National Security, LLC, and shall not be used for advertising or product endorsement purposes.

This work performed under the auspices of the U.S. Department of Energy by Lawrence Livermore National Laboratory under Contract DE-AC52-07NA27344.

FY10 LLNL OMEGA Experimental Programs

In FY10, LLNL conducted several campaigns on the OMEGA laser system and on the EP laser system, as well as campaigns that used the OMEGA and EP beams jointly. Overall LLNL led 301 target shots involving the OMEGA laser system and 96 target shots involving the EP laser system. Approximately 40% of the total number of shots (137 OMEGA shots, 32 EP shots) shots supported the National Ignition Campaign (NIC). The remainder was dedicated to experiments for High-Energy-Density Physics (HED) (164 OMEGA shots, 64 EP shots).

Objectives of the LLNL led NIC campaigns at OMEGA included:

- 1. Reactivation of 4w Thomson scattering diagnostic*
- 2. Study of Bremsstrahlung backlighters for Compton Radiography of ICF implosions*
- 3. Characterization of shell adiabat of spherically imploded inertial fusion-type targets using X-ray Thomson scattering*
- 4. High-resolution measurements of velocity nonuniformities created by microscopic perturbations in NIF ablator materials*
- 5. Equation-of-state measurements of Ge-doped CH*
- 6. Validation of the Compton Radiography diagnostic platform for ICF experiments*
- 7. Experiments to study the physical properties (thermal conductivity) of shocked fusion fuels*
- 8. Characterization of hard x-ray sensitivity of MCP based gated imagers.*
- 9. Characterization of the plasma conditions at the laser entrance hole (LEH) of a gas-filled hohlraum using Thomson scattering.*
- 10. Validation of the modeling of multi-beam scattering occurring in NIC targets.*
- 11. Measurements of the plasma conductivity by means of collective x-ray Thomson scattering*

The LLNL led HED campaigns covered five main areas of research:

1. *Material dynamics and equation-of-state.*
 - a. *Quasi-isentropic compression experiments (ICE) for material properties such as strength, equation of state, phase, and phase-transition kinetics under high pressure.*
 - b. *Platform development using radiographic measurements of instability growth in tantalum to infer material strength using the joint OMEGA-OMEGA-EP configuration*
 - c. *Properties of shocked CH and Si aerogel foams used in high-energy-density experiments*
 - d. *The equation-of-state of a CO₂ mixture along the Hugoniot*
 - e. *Initial experiments to develop an experimental platform to measure the melt and resolidification of Tin*
2. *Opacity*
 - a. *Opacity studies of high-temperature plasmas under LTE conditions*
 - b. *Initial experiments to compare short pulse and long pulse techniques to heat materials to high temperature for opacity data*
3. *Hydrodynamics*
 - a. *Measurements of the Kelvin-Helmholtz instability in laser driven shock tubes*
 - b. *The hydrodynamic evolution of high mach number copper-foam jets*
4. *X-ray source applications*
 - a. *Development of multi-keV x-ray sources for radiography and for the study of material response in samples*
5. *Diagnostic technique development*
 - a. *Development of a target mounted turning mirror for use with the VISAR diagnostic*
 - b. *Demonstration of ultrafast temperature and density measurements with x-ray Thomson scattering from short-pulse laser-heated matter.*
 - c. *Comparison of short pulse and long pulse generated x-ray backlighters*
 - d. *Development of diffraction (white light Laue and powder) to measure the structure of solids (Ta, Fe, Sn)*

This work performed under the auspices of the U.S. Department of Energy by Lawrence Livermore National Laboratory under Contract DE-AC52-07NA27344.

National Ignition Campaign Experiments

4w Thomson Scattering Re-Activation

The 4w Thomson scattering diagnostic was reactivated using a half-day of laser time on the Omega Laser. The diagnostic has been redesigned to measure the high frequency and low-frequency Thomson scattered features. Figure 1 shows the first measurement of Thomson scattering from the electron-plasma wave resonance using a 4w probe beam. The Thomson scattering probe beam is aligned 400 μm off the surface of a Vanadium foil target. The target is heated with a single 3w beam and the 4w probe beam is delayed from the heater beam by 1ns.

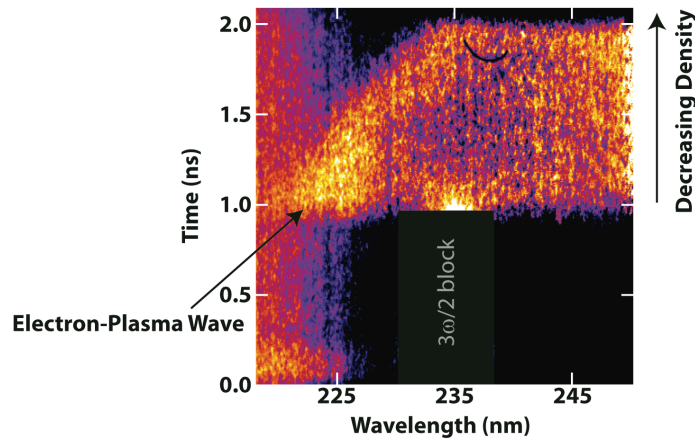


Figure 1: Thomson scattering from the electron-plasma wave resonance.

The wavelength of the Thomson scattered electron feature shown in Figure 1 can be used to measure both the electron temperature and density. The density is decreasing in time due to the expansion of the blow-off plasma, which can be seen in the increasing wavelength of the blue-shifted electron feature.

High resolution Bremsstrahlung backlighters

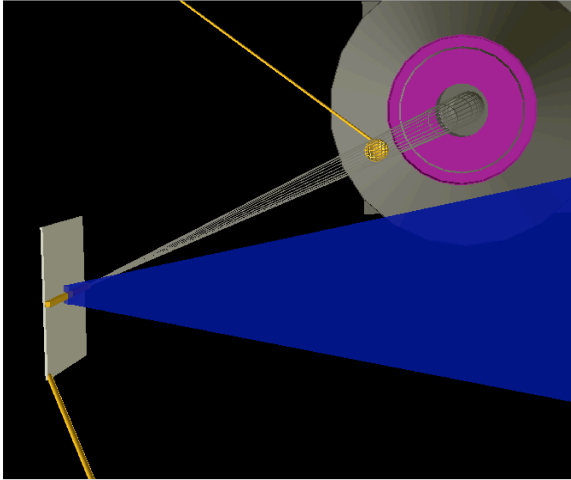


Figure 1: Geometry used in the OMEGA EP target chamber to obtain 2D radiographs of W spheres at photon energies above 75keV. The short pulse beam drives an Au micro-wire on a low-Z substrate

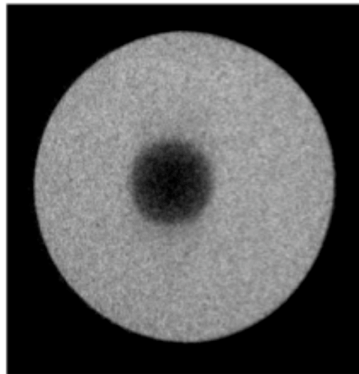


Figure 2: Point projection radiograph of 200μm diameter W sphere using 10μm-diameter Au, micro-wire and 6 Omega beams (1ω), 40J/beam/100ps. The spatial resolution is $\sim 10\mu\text{m}$.

The motivation of the Bremsstrahlung backlighters campaign is to develop and characterize broadband x-ray sources emitting around and above 75keV, to be used in the Compton Radiography of ICF targets. In FY09 we characterized Au micro-wire backlighters irradiated by 10ps-long, OMEGA EP pulses.

In FY10 we characterized Au micro-wire backlighters irradiated by 100ps-long, OMEGA EP pulses (1ω) and OMEGA pulses (3ω), with the primary goal of measuring the effect of longer-pulse generated backlighter with respect to the source size.

As backlighters, we used 10μm diameter, 300μm long, Au wires on a CH substrate, in a point-projection, end-on, geometry. The Bremsstrahlung radiation was generated by irradiating the Au wires with either the OMEGA EP short pulse beam, delivering up to 1000J in 100ps (1ω), or 6 OMEGA short pulse beams, delivering a total of 250J in 100ps (3ω).

As radiography samples we used solid W spheres with diameters of 200μm and 250μm located at a distance of 10mm from the backlighters. In order to record the radiographs and measure the backlighter spectra, we used the Compton Radiography Snout (CRS). A combination of high- and low-Z filters was used inside the snout to restrict the backlit photon energies to above 75 keV. As a detector we used a Fuji BAS imaging plate at about 400mm from the backlighter. The analysis of the radiographs of the W sphere allows the reconstruction of the source size of the backlights. We found no significant difference between 10ps and 100ps EP-produced BL (1ω)

and 100ps OMEGA-produced BL (3ω). In all cases we measured source sizes between 10μm and 12μm. For the experiments performed in the OMEGA EP target chamber, we also deployed the Ultra-Fast X-ray Streak Camera, which provided the durations of the soft x-ray emission from the Au micro-wires of $\sim 12\text{ps}$ and 80ps , for backlighters produced by 10ps and

100ps OMEGA EP pulses, respectively. First results show that the hard x-ray conversion efficiency of the lower intensity 3ω probe is 10-20x less than the 1ω probe as expected. These results pave the way for the implementation of Compton Radiography on NIF, using relatively long pulses and 3w laser irradiation for the backlighters.

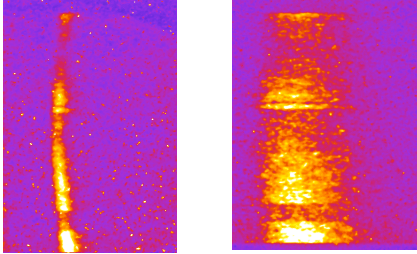


Figure 3: The analysis of the streaked images shows pulse durations of the soft x-ray emission from the Au micro-wires of 12ps (FWHM), when irradiated by 1kJ/10ps (above) and 80ps when irradiated by 1kJ/100ps (below) EP pulses

X-ray Thomson Scattering from Spherically Imploded ICF Ablators

Experiments to characterize spherically imploded inertial fusion-type targets using X-ray Thomson scattering have been recorded at the Omega laser facility in Jan and May of 2010 to study the properties of compressed ICF ablators. Measurement of the temperature and density allows inference of the capsule adiabat, a measure of the plasma pressure to the Fermi pressure, and can be used to test low-adiabat pulse shaping methods.

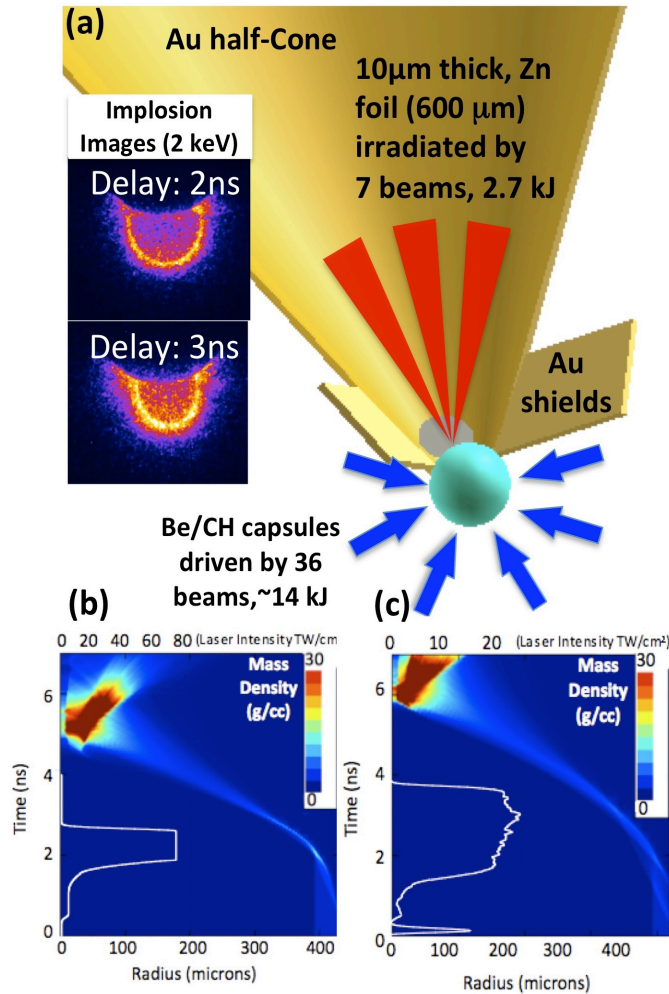


Figure 1: a) Schematic of the experimental set-up. Here, Zn He- α x rays, produced via laser irradiation of a 10 μm thick Zn foil, are scattered from imploding Be and CH capsules that are compressed using 37 additional shaped laser beams. The Zn foil is attached to gold half-cones with Au flaps that shield the detector from the source x rays. Also shown (left) are time-resolved x-ray images of the implosion.

b) (LA2201) & c) (LA370901p) Radiation-hydrodynamic calculations of the mass density, plotted as a function of time and target thickness, where $t=0$ denotes the start of the drive beams. Profiles of the drive-beam waveforms (white) are overlaid on the mass density contour, listed as a function of time and laser intensity.

In these experiments the non-collective, or microscopic, particle behavior of imploding CH and Be shells was probed using a 9 keV Zn He- α x-ray source at scattering angles of 113° and 135° . Figure 1 a) shows a schematic of the experimental setup including time resolved pinhole images of the imploding capsules. The capsules attached to gold half-cones were hemi-spherically driven using 37 drive beams. The Zn He- α probe was created by laser irradiation of a Zn foil positioned on the inside of the Au cone. Figure 1 b) and c) show

radiation hydrodynamic calculations of the mass density as a function of time and radius for the two pulse shapes used in these experiments.

Figure 2 shows scattering spectra from Be(+2) capsules driven with pulse shape LA2201 shown in Fig. 1 b), at 4.2 ns after the start of the drive beams and a scattering angle of 135° . The measured electron density and temperature determined from theoretical fitting to the experimental data was $14 \pm 3 \text{ eV}$ and $1.1 \pm 0.15 \times 10^{24} / \text{cc}$, respectively. For these partially degenerate plasmas, the width of the inelastic Compton feature provides the electron velocity distribution, which is a direct measure of the electron density. The electron temperature is determined from the semi-Gaussian shape of the Compton feature, independent of the choice of structure factor model. Sensitivity of theoretical fitting to the red wing of the Compton feature for varying electron temperatures is shown in Fig. 2. In this geometry, the larger scattering angle of 135° resulted in less dependence of the Compton red wing shape on the finite size of the source and scattering volume, enabling better determination of the temperature and density. Also, this new geometry enabled the use of additional probe beams, which resulted in an increase in signal to noise. These experiments investigate the viability and accuracy in using this diagnostic technique to study the properties of implosion targets at the National Ignition Facility (NIF), LLNL.

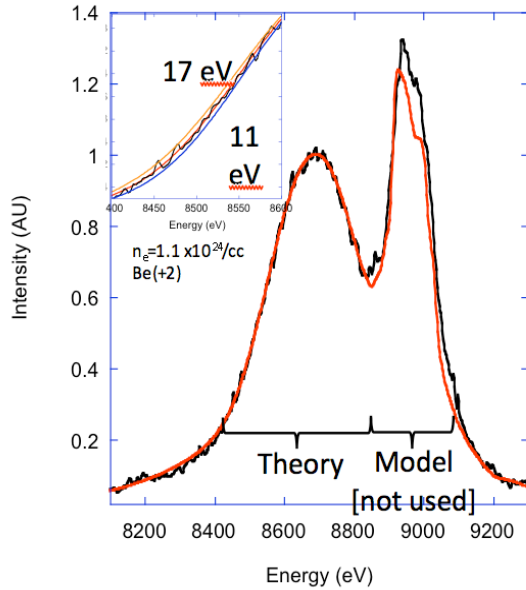


Figure 2. In-flight x-ray Thomson scattering data (4.2 ns) from laser compressed Be cone-in-shell targets (See Fig. 1 b) for the drive pulse shape). Data include an elastically scattered Rayleigh peak at $\sim 9 \text{ keV}$ and an inelastically scattered Compton feature at $\sim 8.7 \text{ keV}$. Theoretical fits to the experimental data yield an electron temperature and density of about 14 eV and $1.1 \times 10^{24} / \text{cc}$, respectively.

High-resolution measurements of velocity non-uniformities created by microscopic perturbations in NIF ablator materials

Two CAPSEED campaigns in FY10 took place in January and March. The primary focus of these campaigns was to produce a survey of clean CH samples, to complete the studies of Be ablator samples and to continue the survey of diamond samples near the melt curve, including the first 2D velocity measurements of shock fronts propagated through single crystal diamond samples. An upgrade to the OHRV diagnostic incorporated vacuum boxes around the interferometers to improve the noise performance of the instrument. The experimental campaigns produced preliminary data on CH, although the data collection was impeded by a pair of previously unencountered problems. During the first campaign inadequate anti-reflection coatings on many of the targets degraded the data quality to the extent that the measurements needed repeating. On the second campaign unconverted light affected the package more than during previous campaigns, owing to a minor design change. Better quality control on the anti-reflection coatings solved the first problem, and a new shield design to mitigate the unconverted light issue has already been tested successfully (on a later non-CAPSEED campaign). The study of the Be ablators was completed during these campaigns, with the new data confirming results achieved previously. A highlight of the Capseed-10B campaign was the observation that the shock front of a ~ 500 GPa shock front in a single crystal diamond sample (below melt) was highly roughened, equivalent to the previous observations on polycrystalline diamond, thus suggesting that the processes leading to the roughening are an intrinsic property of diamond.

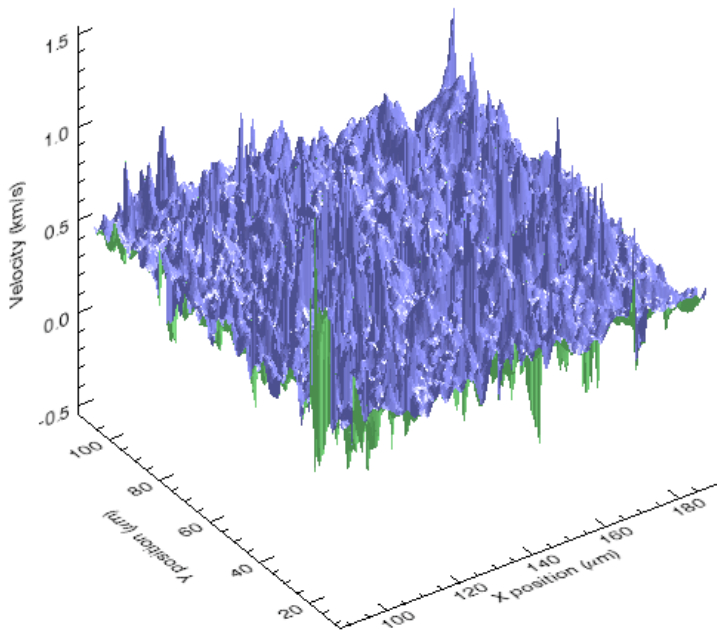
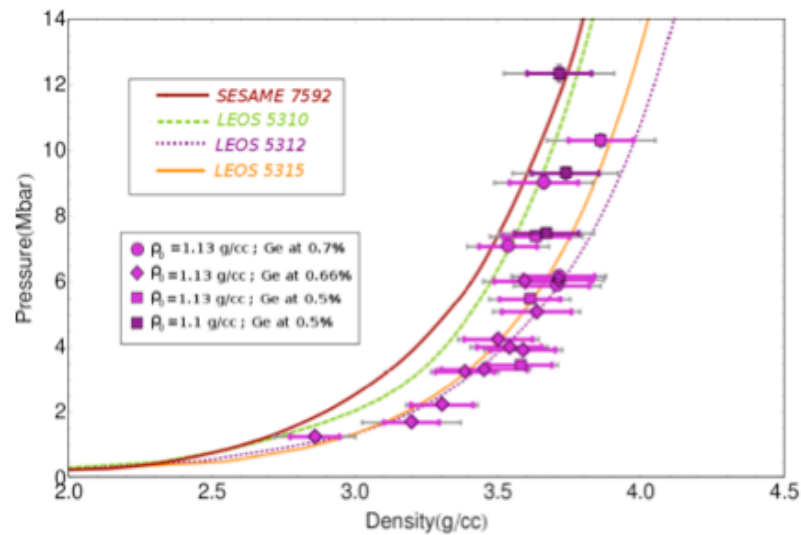


Figure 1: Two-dimensional velocity fluctuations over a $100 \times 100 \mu\text{m}^2$ region of a ~ 500 GPa shock front traveling through a single crystal diamond sample with $\langle 100 \rangle$ orientation.

Equation-of-state measurements of Ge-doped

Knowledge of the equation-of-state (EOS) of NIF ablator materials is important to correctly predict shock timing in an implosion. Plastic ablators in current NIF capsules are composed of layers of pure and Germanium-doped $\text{CH}_{1.3}$. Recent shock Hugoniot measurements on both CH and CH_2 showed good agreement with models between 1-10 Mbar, providing confidence in the EOS for undoped plastic. In FY10, new shock Hugoniot measurements were performed on Ge-doped $\text{CH}_{1.3}$. Using impedance matching to a quartz standard the pressure and density of several samples doped with between 0.5 and 0.7 atomic % Ge were measured. These data, supplemented by additional data from LLE shots, are shown in the figure below. From 1-6 Mbar the data are in good agreement with LEOS 5315 (0.5% Ge) and LEOS 5315 (0.2% Ge) – models currently being used in simulations of NIF implosions – but are less compressible than these models at higher pressures (for comparison, two models for pure CH (Sesame 7592 and LEOS5310) are shown). Although it is unclear why there is a tendency toward stiffer behavior above 6 Mbar, the agreement in the 2-3 Mbar range corresponding to NIF first shocks justifies the use of these EOS tables in current simulations.



Compton Radiography

The goal of the Compton Radiography campaign is to build a novel diagnostic platform for ICF for the characterization of shape and density of the fuel in ICF implosions. After having successfully demonstrated Compton Radiography of implosions in FY09, in FY10 we applied Compton Radiography to three kinds of implosions.

In the first experiment we used 60 beams of the OMEGA laser facility to directly drive implosions of 40 μ m thick, 870 μ m diameter CH capsules filled with 8atm DD gas, located at the target chamber center of OMEGA. As a backlighter we used a 10 μ m diameter Au wire, 300 μ m long, in a point-projection, end-on, geometry at 10mm distance from the CH shell. The backlighter was driven by the OMEGA EP short pulse beam, delivering \sim 1kJ at 10ps in a 100 μ m square spot size.

The time delay between the OMEGA EP short pulse and the OMEGA laser pulses was varied in order to bracket the peak compression time predicted by LILAC 1D simulations. As an example, Fig.1 shows a radiograph of the imploding CH shell, near peak compression, obtained at a photon energy of \sim 100keV, where Compton effects dominates the fuel opacity. The radiograph, having about 10ps and 10 μ m, temporal and spatial resolution, respectively, shows a limb-darkened shell of about 90 μ m diameter.

In a second experiment we successfully recorded radiographs at photon energies $\langle h\nu \rangle \sim$ 70keV, of 54 OMEGA beam direct-drive implosions of cone-in empty CD shells and 60 OMEGA beam direct-drive implosions of empty CD shells, without cones. Again, the Au micro-wire backlighters, with 10ps and 10 μ m, temporal and spatial resolution, respectively, were driven by the OMEGA EP short pulse beam, delivering \sim 750J at 10ps in a 100 μ m square spot size. The radiographs of cone-in shell implosions show the shell near peak compression, at a distance of 50 μ m and having a diameter of about 50 μ m. Our third experiment was dedicated to recording Compton radiographs of cryogenic direct-drive implosions. This effort is a work in progress as the experimental setup imposes very tight tolerances on the alignment of the target and backlighter and relies on an improvement of the cryogenic target alignment system. The CompRad campaigns fully validated a novel diagnostic technique, Compton Radiography, that will be extremely useful when implemented on NIF implosions.

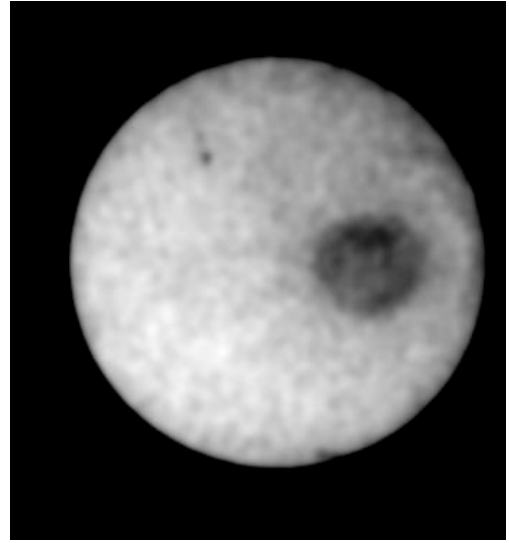


Figure 1: *Compton Radiograph of 870 μ m- diameter CH capsule filled with 8atm DD, near peak compression. The radiograph has been recorded at an effective photon energy $\langle h\nu \rangle \sim$ 100keV, where Compton effects dominates the fuel opacity. The radiograph shows an object about 90 μ m in diameter inside the shadow of Compton Radiography Snout collimator.*

Conductivity of D₂ and CH

The thermal transport properties of D₂ and CH at high densities have important implications for the stability of ICF implosions. The OMEGA laser is used to prepare off-Hugoniot states of these materials using multi-shock compression. Pressure, density, temperature, and optical properties of the compressed materials are determined by simultaneous VISAR and SOP measurements. D₂ states up to 10 Mbar and 3 g/cc have been achieved at temperatures below 1 eV. CH states up to 8 MBar and 4.5 g/cc have been achieved at temperatures near 3 eV. A Drude-like model is used to infer band gap closure and electrical and thermal conductivities from the optical behavior at different states. Preliminary results indicate that D₂ thermal conductivity at such high density, low temperature states may be well below theoretical predictions.

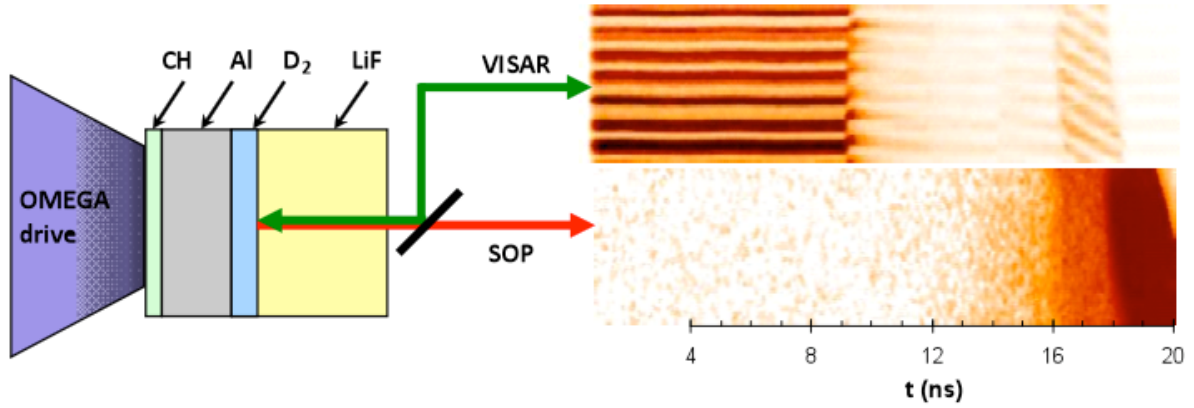


Figure 1. A sequence of three OMEGA laser driven shocks is sent into a thin layer of liquid D₂ trapped between an Al pusher and a LiF window. For the states reached in this experiment, the LiF remains transparent, and the VISAR and SOP records track the velocity, reflectance and optical emission of the D₂-LiF interface. A dramatic increase in the D₂ reflectance is observed upon the arrival of the third shock at this interface (at ~16 ns), corresponding to a large increase in the conductivity. The three shocks coalesce in the LiF at about 18 ns, increasing the LiF temperature and ending its transparency.

Characterization of hard x-ray sensitivity of MCP based gated imagers

An MCP based gated x-ray imager is one of the most important diagnostics of the National Ignition Campaign. In FY09, we characterized neutron-induced background of the MCP based x-ray imagers with a CCD (Kodak KA-16801E) and a photographic-film readout (TMAX 3200) on OMEGA high neutron yield shots [1]. In FY10, we assembled a new MCP based x-ray framing camera: “radiation hardened Gated X-ray Imager” (hGXI) and tested its x-ray sensitivity at OMEGA laser facility.

In order to optimize experimental setup of NIF implosion experiments, it is crucial to know

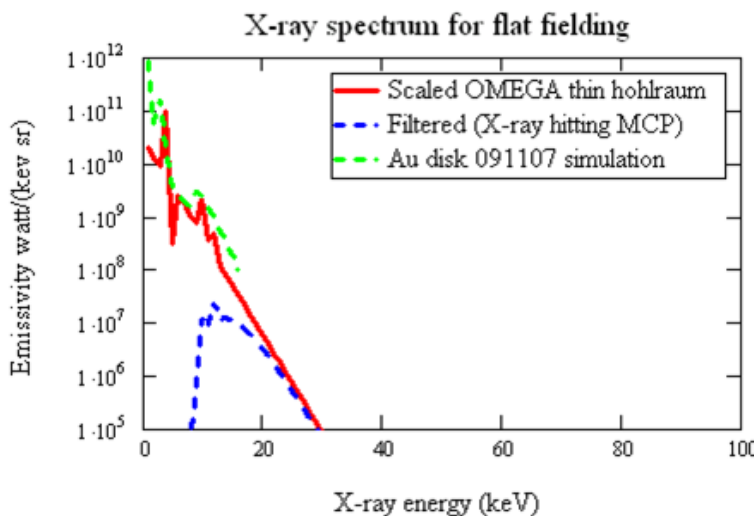


Figure 1: X-ray production from the gold sphere. X-ray conversion efficiency was estimated by a radiation-hydro simulation and extrapolating x-ray spectra of previous experiments

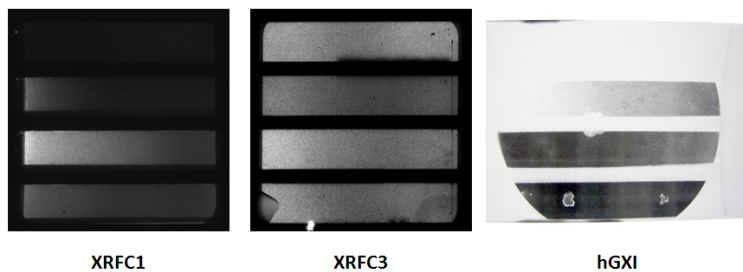


Figure 2: Images obtained with flat fielding experiment.

this experiment. The signal intensity obtained by those cameras (hGXI: OD = 1.97, 193

absolute sensitivity of the gated x-ray imager for 10~20 keV x-ray. To test x-ray sensitivity in this energy region, we performed calibration experiments at OMEGA laser facility.

A gold-coated spherical target (diameter: 1.015 mm) was irradiated by 60 laser beams (UV, 500J/beam, 1ns square pulse). The laser intensity on the sphere was $1.2 \times 10^{15} \text{ W/cm}^2$. Absolute x-ray emission spectrum was recorded by x-ray spectrometers (HENWAY and DCS). In order to compare relative sensitivities, 3 different gated x-ray imagers (hGXI, XRFC1, XRFC3) were located 1600 mm from the target chamber center. In front of the MCP, a 2.5mm thick polyimide and 0.6mm thick aluminum filter was used to cut off low-energy component ($<7 \text{ keV}$) and attenuate the x-ray fluence. Fig 1 shows estimated x-ray production on the target and spectrum through the filters. The estimated x-ray flux on the MCP is $2.5 \sim 5 \text{ kW/cm}^2$. Fig. 2 shows images obtained with

merg/cm², XRFC1:1250 ADU/pix, XRFC3: 1750 ADU/pix) was consistent with our numerical model. Those numbers will be used for benchmarking of the MCP model.

[1] N. Izumi et al., accepted for publication on Rev. Sci. Instrum. 81 (2010)

Plasma characterization of the LEH region of Gas-filled Hohlraums

The objective of this campaign was to characterize the plasma conditions at the laser entrance hole (LEH) of a gas-filled hohlraum using Thomson scattering. This region is of special interest for crossed-beam energy transfer which is a process that can transfer a large percentage of laser energy between beam cones. The energy transfer is governed by the electron temperature, plasma flow velocity, and laser beam wavelength. Thomson scattering measurements from the ion feature were made for a series of hohlraums with LEH diameters of 800, 1000, and 1200 μm , Figure 1.

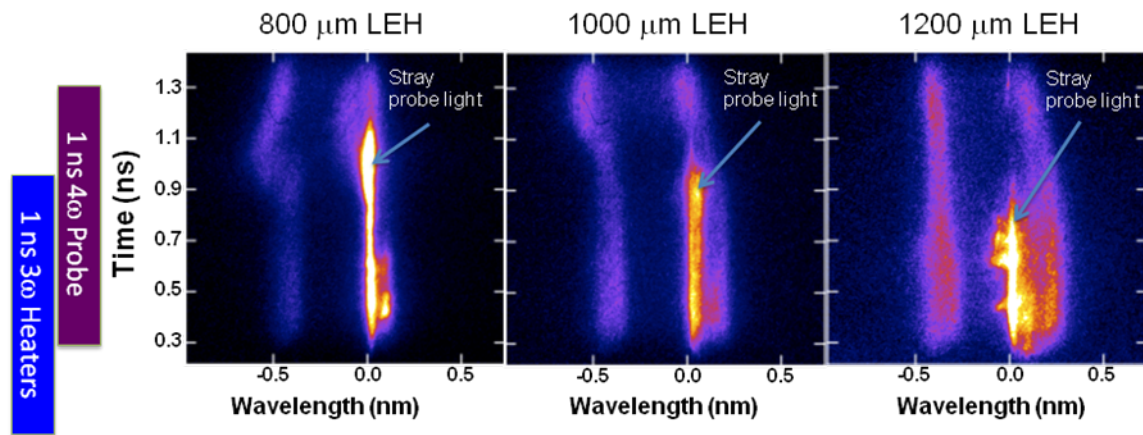


Figure 1: Thomson scattering measurements of the LEH region of a gas-filled hohlraum.

The Thomson scattering measurements are compared to hydrodynamic simulations using the code HYDRA in Figure 2. The plasma flow velocity is shown for three different locations along the simulation hohlraum axis. Large gradients in this region are predicted by the modeling. The measured electron temperature and flow velocity will be used to benchmark different heat transport models.

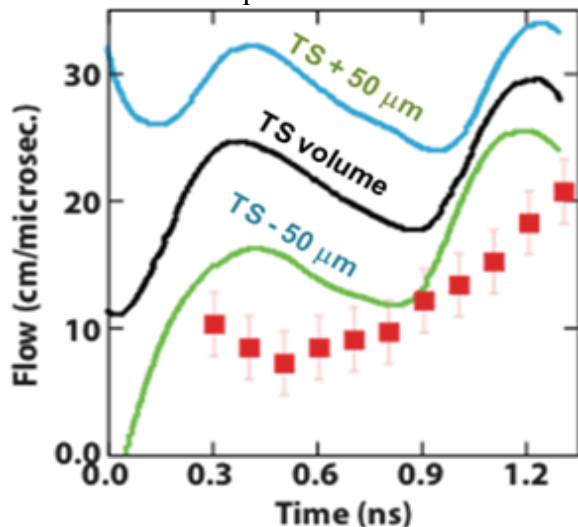


Figure 2 : The experimental measures (red squares) are compared to hydrodynamic simulations at different locations outside the LEH.

Validation of the modeling of multi-beam scattering occurring in NIC targets

A series of experiments were carried out to verify a critical component of the model of backscatter from the multiple NIC beams which indicates that backscatter from the interior of the hohlraum can be amplified by each of the crossing beams it encounters as it exits the laser entrance hole. The model predicts that even with a small gain exponent from each of several crossing beams, the over all gain exponent, and amplification, produced by all the beams can be quite significant with the gain exponents of linear waves adding. The Omega experiments used a 3 micron thick CH foil target illuminated with 28 heaters beams to produce plasma conditions similar to what is found in NIC ignition targets, and the Mach 1 flow velocity that is necessary to produce resonant amplification of a seed with the same wavelength as the pumps, as shown in figure 1.

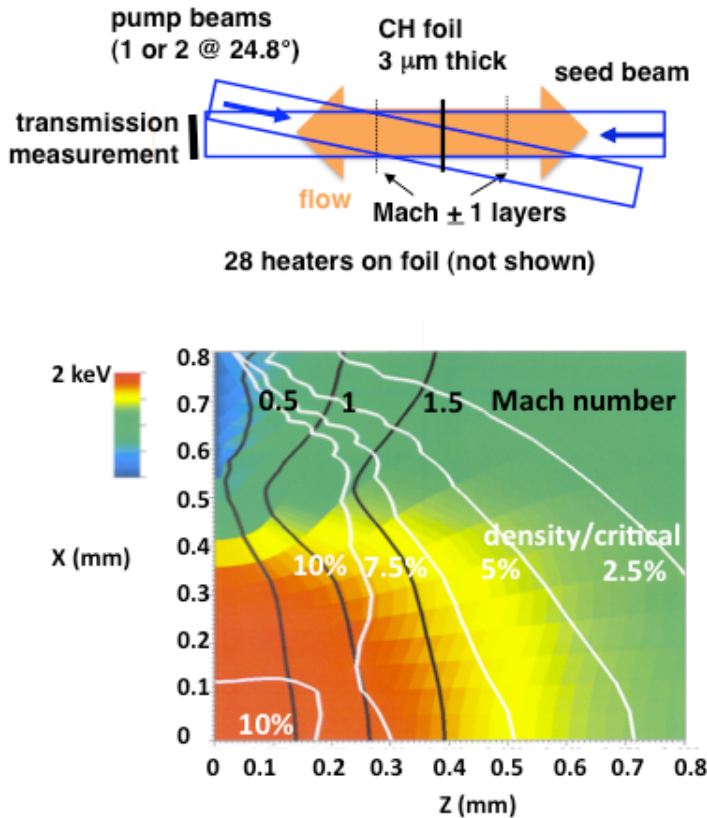


Figure 1 : The experimental geometry of a foil target used to produce the plasma conditions and Mach 1 flow, shown at 1.4 ns, that is necessary for resonant amplification of a seed of 351 nm light representing the SBS backscatter produced in the interior of the NIC hohlraum.

Experiments were performed in which the transmission of a seed beam (B46) was measured in the case of no, one, and two crossing pump beams (B30, B50), and the transmitted power in each case is shown in figure 2.

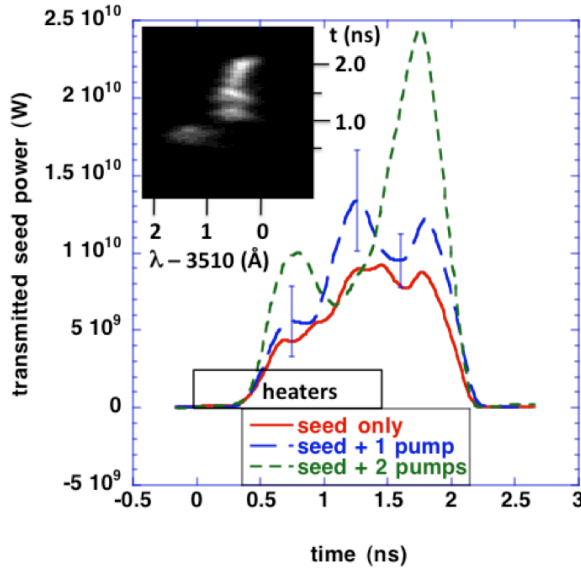


Figure 2: Streaked spectrum and transmitted power waveforms of the seed beam transiting the foil target plasma, for the case of; no amplifying pump, and one and two amplifying pumps, showing enhancements in the seed power produced by energy transfer from the pumps to the seed beam.

Note that a single pump beam produces enhanced transmission relative to the no pump case near 1.4 ns, as expected from the simulations of the resonance conditions, and a second pump beam produces an even greater increase in the power at a somewhat later time. These results were obtained at three different seed intensities and similar amplifications were found in each case, consistent with a linear ion acoustic wave response. Further experiments were carried out to demonstrate the control of energy and power transfer by the relative alignment of the polarization vectors of the pump and seed beam, as shown in figure 3.

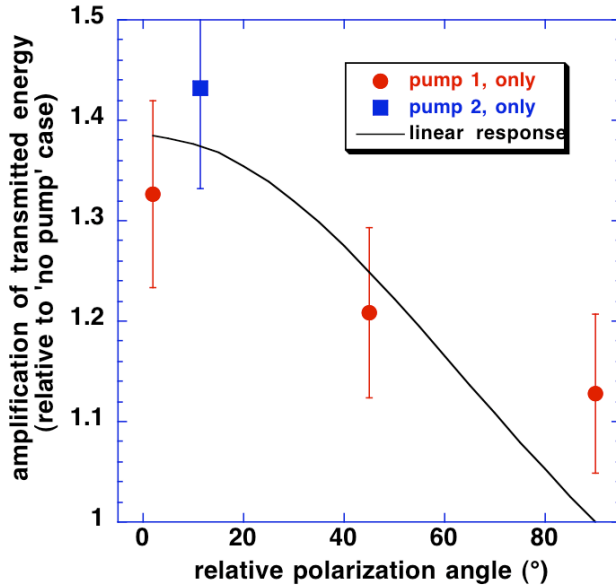


Figure 3: Energy amplification factor produced by a single pump beam as a function of its polarization angle relative to the seed beam.

To change the polarization the $\frac{1}{2}$ wave plate, or polarization rotator, was installed in B50 and its polarization was rotated through 90° with respect to the seed beam polarization. The experiments demonstrated greatest amplification when the polarizations were aligned, as determined from the energy amplification factor measured in three experiments and shown in figure 3. The greatly reduced amplification when the polarization angle was near 90° demonstrates the importance of relative polarization in controlling this effect. This work has increased the confidence in the modeling of multi-beam scattering occurring in NIC targets.

Measurements of the plasma conductivity by means of collective x-ray Thomson scattering

The goal of this experiment was to measure the electron-ion collision frequency n_{ei} in isochorically heated beryllium from the broadening of plasmon signals measured with x-ray Thomson scattering [Döppner *et al.*, J. Phys.: Conf. Series (2010)]. n_{ei} is directly related to the conductivity which is an important parameter to correctly model capsule implosions on the NIF; at the same time it is only known with great uncertainty from theoretical predictions.

On this joint Omega – Omega EP shot day we utilized the Omega EP beam (250 J in 10 ps) to isochorically heat a Be cube with 200 micron side length to 35 eV, assuming 20% conversion efficiency into hot electrons ($T_{hot} \sim 200$ keV), as shown in Fig. 1a. The Be front surface, which gets much hotter, is not seen by the scattering experiment due to proper shielding. The size of the gold shields is chosen such that plasma moving around the shield and still emitting line radiation will be imaged to the detector well separated from the scattering signal. This is important because we cannot use gated detectors in this short-pulse environment. 14 Omega beams at 3w drive a 12-micron thick Saran foil to create the Cl Ly-a probe line at 2.96 keV. We chose a pulse width of 200 ps to achieve a good time resolution of the scattering experiment. Rad-hydro simulations show that at temperatures of few 10 eV the Be cube does not disintegrate within the first 750 ps. The scattering angle was at 30° to ensure a large collectivity parameter $a \sim 1.7$, necessary to observe plasmon broadening due to collisions.

To measure the scattering spectrum we developed a new high efficiency Bragg crystal spectrometer in von-Hamos geometry, utilizing a cylindrical curved HOPG crystal (see Fig. 1b). The signal is recorded on image plates. The CLVH spectrometer was successfully fielded for the first on this shot day. For cross-calibration, and as source monitors we additionally monitored the Cl K-shell emission with the GTS and XRS1 spectrometers, operated with image plates, and with SSCA on the Omega-only shots.

We had a total of 9 shots, which included 3 joint shots at full energy, 2 EP-only, and 4 Omega-only shots. On the low energy qualification shot of the Omega EP beam we used the emission from an Au-coated CH sphere to measure the timing between the Omega and Omega EP lasers, and establish a delay of 400 ps of the Omega probe beams with respect to the Omega EP beam. During the day we varied the conditions to create the x-ray probe. On most of the targets, the Saran foil had a 30 micron Polypropylene backing to prevent Cl containing plasma moving into the line of sight of the CLVH spectrometer above the Be cube, and obscure the scattering signal. In combination with the low backlighter drive energy (~ 1 kJ in 0.2 ns compared to ~ 7.5 kJ in 1 ns for other XRTS platforms) we were not able to observe a scattering signal. The strongest signal was obtained for a target which had no Poly Propylene backing, and increasing the Omega pulse length to 600 ps, as shown in Fig. 1c.

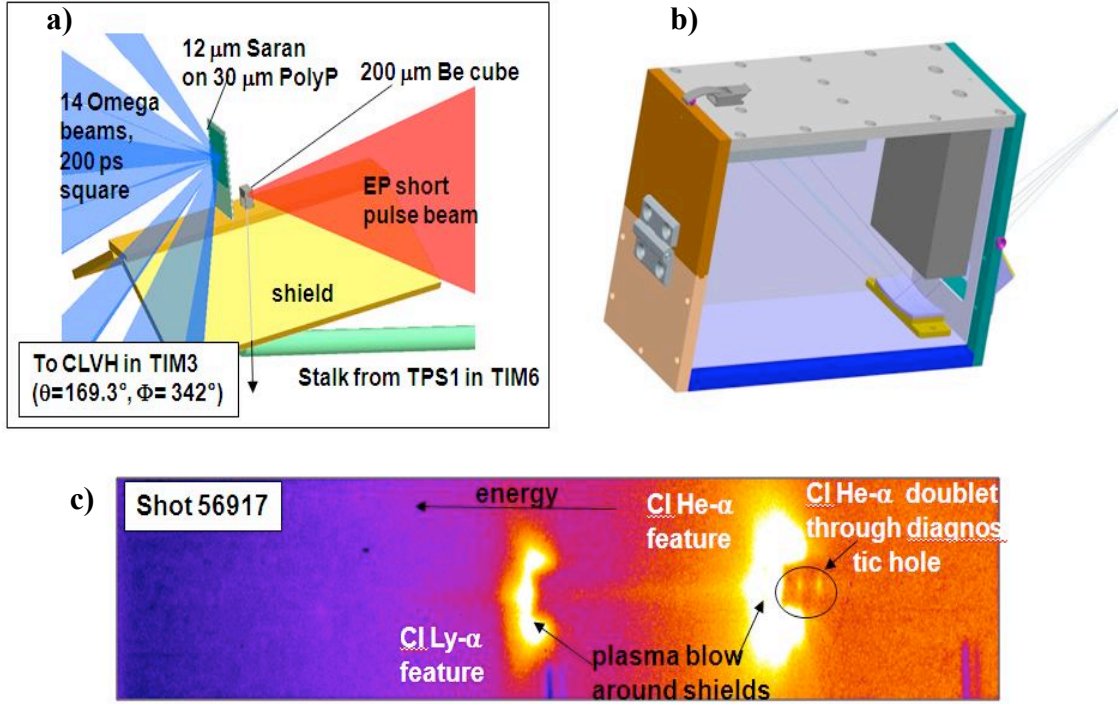


Figure 1: a) Experimental setup to isochorically heat a 200 μm Be cube and characterize the plasma conditions with x-ray Thomson scattering using the Cl Ly-α line at 2.96 keV. b) The CLVH spectrometer, utilizing a cylindrical curved HOPG crystal in von-Hamos geometry to achieve high detection efficiency, was developed for this campaign, and successfully fielded for the first time. c) Data from CLVH.

The most prominent features are due to Cl He-α and Cl Ly-α emission from plasma that is moving around the shields. In the non-dispersive axis the spectrometer is imaging with $M = 1$, and the extension of the shields of $\sim \pm 3$ mm from the center axis can clearly be seen. X-ray emission from the direction of the Be cube at TCC is imaged to the central axis. Clearly, a weak Bremsstrahlung signal and the He-α doublet can be identified originating from that direction.

High-Energy-Density Experiments

I Material Dynamics and Equation-of-state

Iron Equation of State: Ramp compression of Fe to 300 GPa

The preliminary design for a ramp compression experiment on iron (Fe) up to 300GPa is shown in the upper right image in Figure 1, along with the ramp laser pulse shape as calculated by a radiation-hydrodynamics code (lower right). The ramped laser pulse shape for the 36 beams focused onto the inner walls of the hohlraum results in a time-dependence in the radiation temperature and subsequently a ramp-compression wave is launched into the stepped Fe sample. The resultant raw VISAR data and the extracted free-surface velocity $U_{fs}(time)$ profiles for 25.5/21.9/38 μm thick Fe samples are shown on the left in Figure 1.

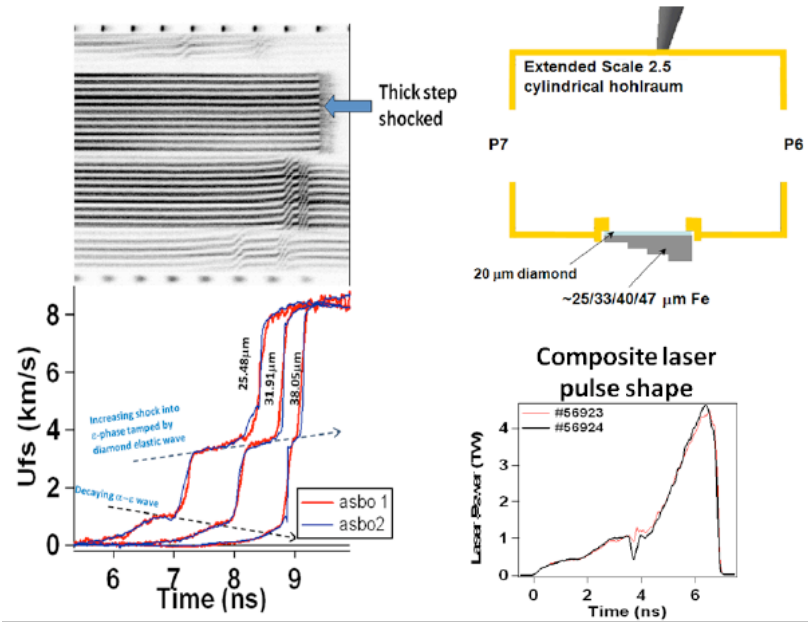


Figure 1 - Preliminary attempts to ramp compress multi-stepped Fe samples to a peak stress of ~ 300 GPa where successful. However strong time-dependence was observed associated with compression across the $\alpha \rightarrow \epsilon$ phase boundary.

The $U_{fs}(t)$ profiles reveal a strong rate dependence associated with the α - ϵ structural phase transformation. The equilibrium pressure for this transformation as measured in shock compression experiments with mm-thick samples is 13 GPa. However the measured pressure for the α - ϵ phase transformation in these experiments for thin samples and high strain rates is ~ 20 GPa. This strong time dependence compromises the extraction of stress-density data using the standard ramp compression analysis techniques. To overcome this difficulty subsequent experiments have been designed such that a steady initial ~ 70 GPa shock is launched into the stepped Fe sample followed by subsequent ramp compression to ~ 300 -400 GPa. This initial shock compresses directly into the ϵ -phase by overdriving the α - ϵ phase transformation and therefore avoids the complications associated by the kinetics of this transformation. With the high-pressure ramp compression platform developed during this period we have demonstrated

compression of solid Fe to peak stresses of 300GPa, and detected and observed strong time-dependence in the structural phase transformations.

Boron Ablator for quasi-isentropic compression experiments

The purpose of this campaign was to demonstrate the performance of boron as an ablator. By measuring the shock break times of a stepped reservoir, we can deduce the ablation pressure created by the ablator material. Our data matched well with the LASNEX simulation with ablation pressure of 52 Mbar, which will be sufficient to create up to 5 Mbar pressure for the quasi-isentropic drive for the material strength Rayleigh-Taylor experiments on NIF.

Tantalum Rayleigh-Taylor Experiments

The goal of the ICETaRT experiments is to measure the dynamic properties of solid-state tantalum (Ta) under high pressures (>1 Mbar) and high strain rates ($10^6 - 10^8 \text{ sec}^{-1}$) using the Rayleigh-Taylor (RT) instability. We achieve quasi-isentropic high-pressure conditions by utilizing a unique plasma piston configuration where the sample materials stay well below the melting temperature while they are plastically deformed under high pressure, as shown in Figure 1. We have measured the growth of the RT instability in vanadium [1] and tantalum, and used this data to compare with predictions using different material strength models. The amount of growth is measured by face-on radiography using laser-driven x-ray backlighters. In order to probe high-Z materials such as tantalum, we use high-energy backlighter x-rays of 20 to 50 keV generated by the Omega-EP beam.

The experiment is conducted in the main Omega chamber in the joint Omega- Omega EP

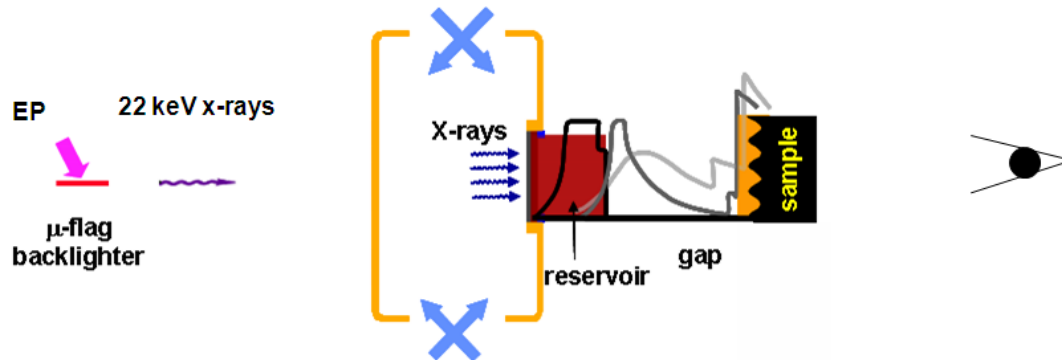


Figure 1 - ICETaRT experiment configuration for an Omega/Omega-EP joint shot

shot configuration. We have obtained a series of successful radiographs from these

experiments. Figure 2(a) shows one example of a face-on 22 keV x-ray radiograph of a rippled sample target of tantalum at 60 ns after initial laser pulse. The driven ripples constitute the circular central part of the image, while the upper portion of the image contains calibration features (stepped filters and knife-edge resolution block) to aid in the extraction of the growth factor. The ripple amplitudes are derived from transmission contrast between the peak and valley of the ripple regions. Our initial growth factor measurements are compared to many strength models (Figure 2(b)), including the new Ta multiscale model that starts with a quantum mechanical interatomic potential and is based on the motion and multiplication of dislocations [2], and the Preston-Tonks-Wallace (PTW) strength model [3].

Our experiments later in the year addressed the effect grain size (Hall-Petch effect) had on the strength under these high pressure and high strain rate conditions. While there are many

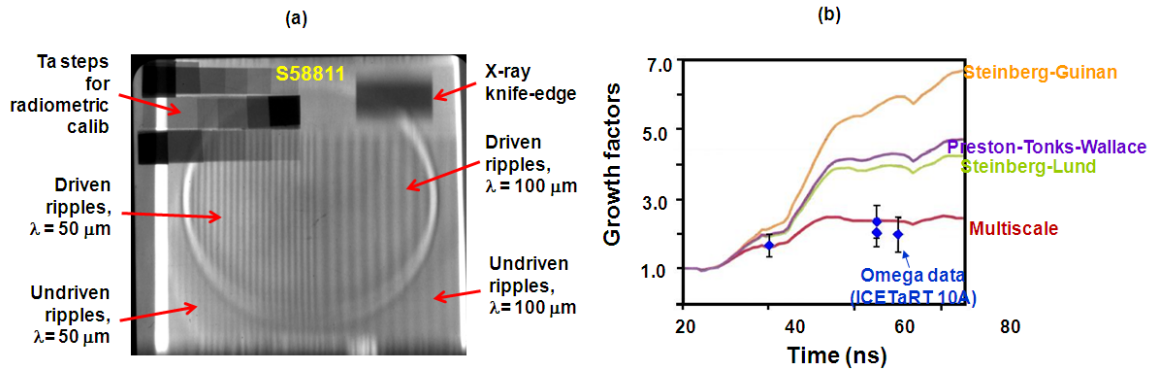


Figure 2 - (a) Face-on 22 keV x-ray radiograph of a rippled sample target of tantalum at 60 ns after the initial laser drive. The driven ripples constitute the center of the image, while the upper portion of the image contains added features (stepped filters and knife-edge resolution block) to aid in the extraction of the growth factor. The ripple amplitudes are derived from transmission contrast between the peak and valley of the ripple regions. (b) Comparison of various model predictions with growth factor data. The data reach peak pressures between 1.2 and 1.4 Mbar and average strain rates around $2 \times 10^7 \text{ s}^{-1}$.

measurements of the Hall-Petch effect at ambient conditions, where strength varies as (grain-size)^{-1/2} [4], no previous theory or experimental measurements under high pressure, high strain rate dynamic conditions existed. We fabricated 3 different types of target that have average grain sizes of 90 microns, 15 microns and 0.25 microns, as shown in Figure 3(a). The radiography data quality was very high and we obtained useful data on all shots. The strength is inversely related to the RT growth factor, which is shown as a function of the average grain size in Figure 3(b). Within the error bars of our data, no obvious Hall-Petch effect is observed. The data analysis is still in progress to understand the theoretical and physical implications our results.

- [1] H. S. Park et al., PRL. 104, 135504 (2010); H.S. Park et al., PoP 17, 056314 (2010).
 [2] N.R. Barton et al., J. Appl. Phys., submitted (Sept. 2010).
 [3] D.L. Preston, D.L. Tonks, and D.C. Wallace, J. Appl. Physics 93, 211 (2003).
 [4] M. A. Meyers et al., Prog. Mater. Sci. 51, 427 (2006).

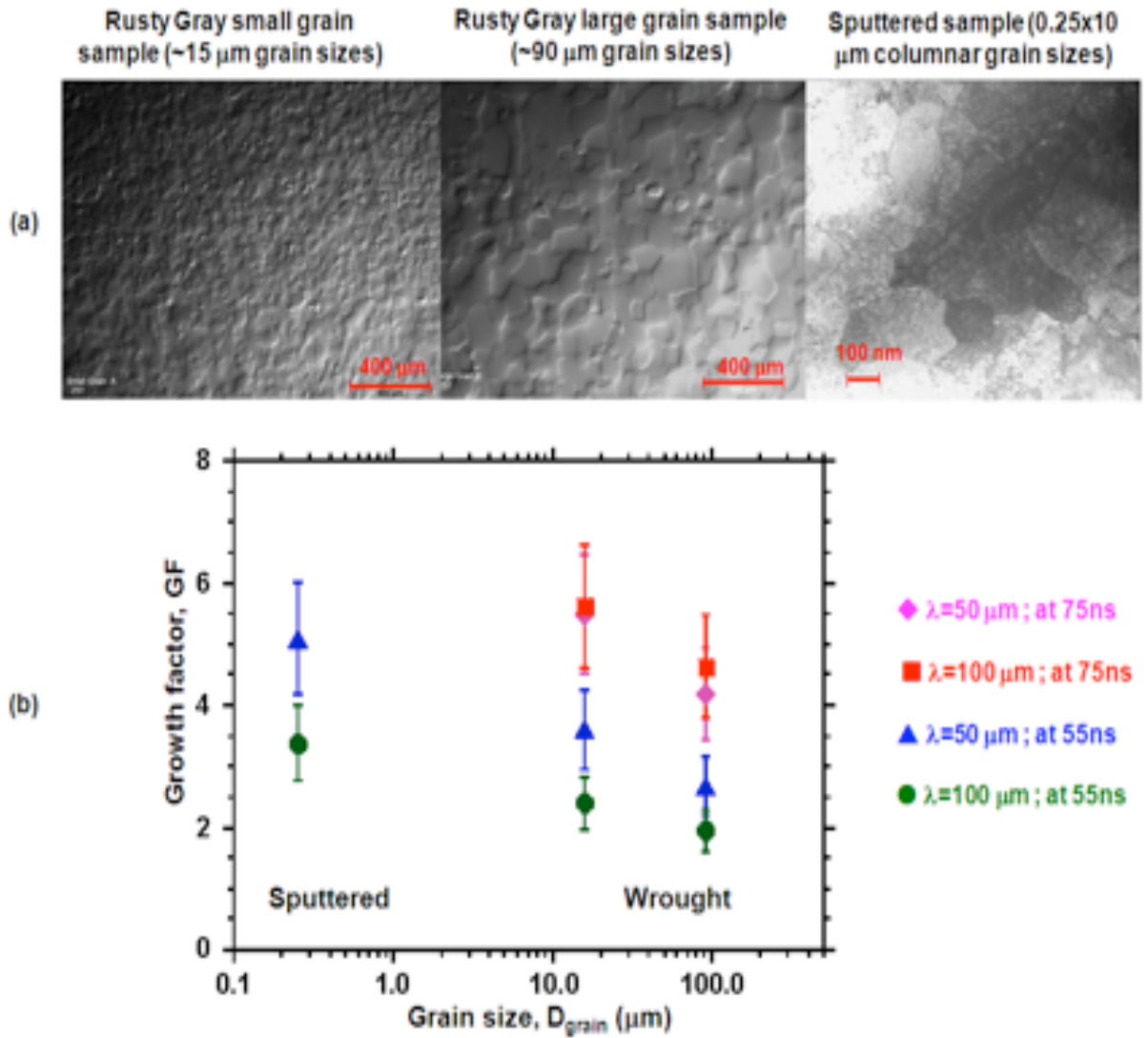


Figure 3 - (a) SEM and TEM pictures of the different Ta grain size samples. (b) Growth factor, which is sensitive to material strength, as function of grain size. No obvious Hall-Petch effect is observed.

Si aerogel foam equation-of-state

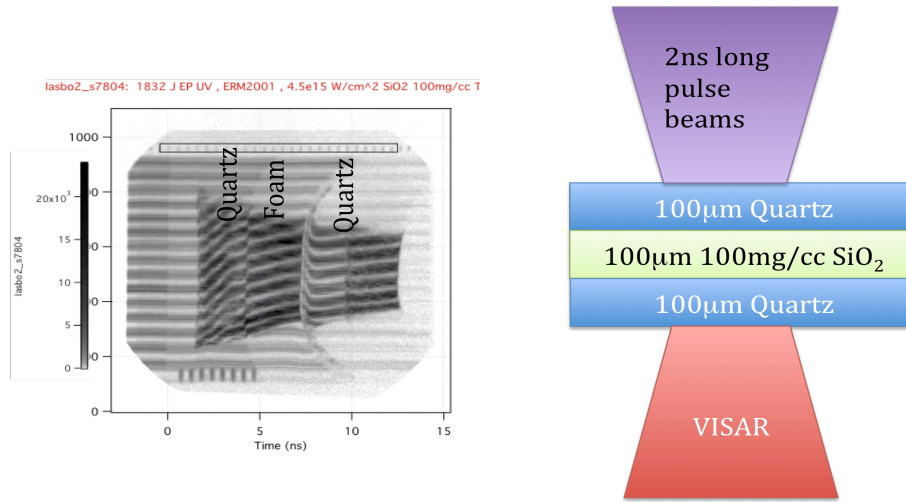


Figure 1 - Target geometry and example data. The VISAR trace shown follows the shock wave through the quartz and 100mg/cc SiO₂ aerogel.

The study of the equation of state (EOS) of low density foams allows one to achieve states of matter with high temperatures at lower than solid density. These conditions appeal to a range of interest for high energy density science.

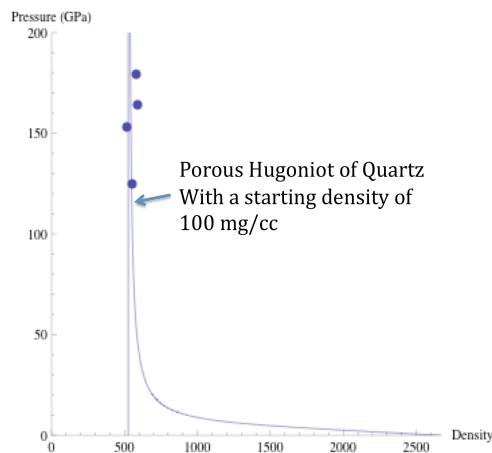


Figure 2 - Plotting the pressure density points compared to a model prediction of the shock Hugoniot of 100 mg/cc SiO₂ aerogel.

determine the properties of the foam. Figure 2, is a plot of data taken over four shots at a single initial density. The large increase in density at low pressures is due to the compaction

of matter with high temperatures at lower than solid density. These conditions appeal to a range of interest for high energy density science. Foams at different densities can be used in EOS experiments to study points along unloading isentropes, which allows material EOS studies of the Hugoniot. Foams also play an important role in laboratory based astrophysical experiments like supercritical radiative shocks or simulate supernovae remnants formation. All of these uses of foams require a detailed understanding of the EOS of the foam itself. Unlike other material EOS studies, which vary pressure and temperature, the foam has an adjustable initial density that plays a key roll in determining the material behavior. In these experiments we place the foam of interest, in this case 100 mg/cc SiO₂ aerogel between two quartz plates, as shown in Fig 1. A decaying shock wave is launched through one of the quartz plates and the propagation of the reflecting shock front through the quartz and foam is followed by an optical VISAR system. In this system the known Hugoniot of the quartz is used with an impedance matching model to

of voids in the material, at the higher shock pressures the compaction of the voids causes heating and the majority of the pressure is due to thermal pressure.

CH Foam Shock Breakout Experiment

Understanding the behavior of foams in the presence of a strong shock is an ongoing effort at several institutions. We performed a series of experiments to investigate the material properties of a new foam material, dicyclopentadiene ($C_{10}H_{12}$), at a density of 40 mg/cc. The targets were configured as shown in Figure 1, and were driven by 15 beams with a pulse length of 1 ns. Some targets were driven with a plastic (CH) ablator and an Al piston, and some used a Cu foam piston (density 0.9 g/cc).

The primary diagnostic was VISAR (including the streaked optical pyrometer [SOP]), which was used to measure the shock breakout. Data from these shots are shown in Figure 2. The shock in the foam at full drive (5488 J) showed dramatic evidence of preheat (presumed to be drive x rays preheating the foam), although the shock in the quartz was measureable as may be seen in the left image in Figure 2. With significantly reduced drive (3057 J), shock breakout from the foam was observed (see right image in Fig. 2). This experimental series has been put on hold as we are evaluating the mechanical properties of the material for fabricating targets. These were the first targets fabricated from DCPD, and the material appears to have less rigidity than hoped.

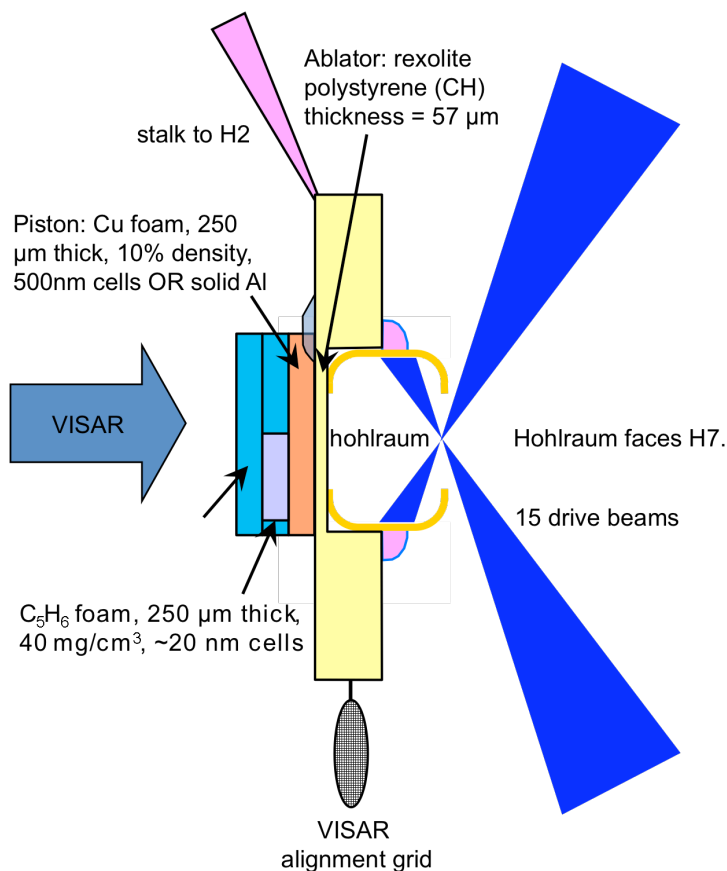


Figure 1 - Target, laser, and diagnostic configuration for the CH Foam Shock Breakout campaign.

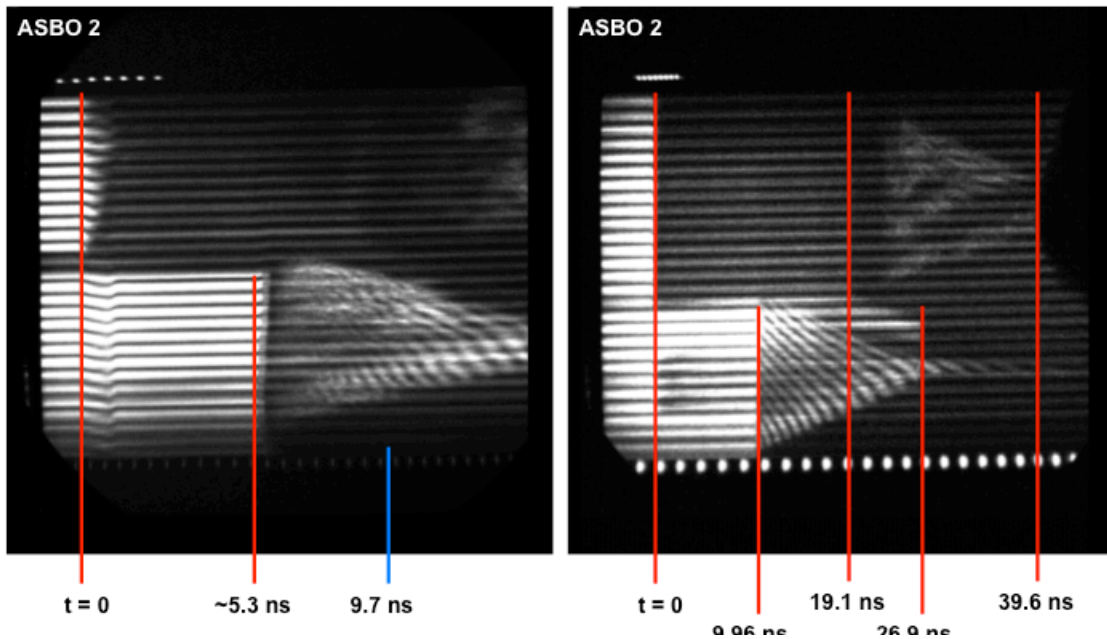


Figure 2 - (left) VISAR signal from the target shown in Figure 1, driven with 5488 J. No shock breakout is visible in the top of the image, and the reflected signal appears to only be from the back surface of the quartz anvil. (right) VISAR signal from a similar target driven with 3057 J. The shock breaks out of the $C_{10}H_{12}$ at about 19.1 ns and is visible in the quartz anvil before breaking out at 39.6 ns.

CO₂ Hugoniot measurements to 950 GPa

CO₂ EOS is of wide scientific interest. It is found in the core of giant planets. It is a mixture, which challenges models to accurately predict. Prior experimental data were limited to below 100 GPa. Experimental measurement of the CO₂ Hugoniot was extended up to 950 GPa by launching shocks into CO₂ samples pre-compressed in diamond anvil cells to ~0.5 GPa, see Figure 1. VISAR and SOP measurements of the CO₂ shock front in comparison to concomitant measurements in quartz were used to infer pressure, density, reflectance, and temperature of shocked CO₂. CO₂ shock reflectance saturated at about 35% above 350 GPa, and the pressure, density, and temperature results are consistent with the theoretical LEOS table.

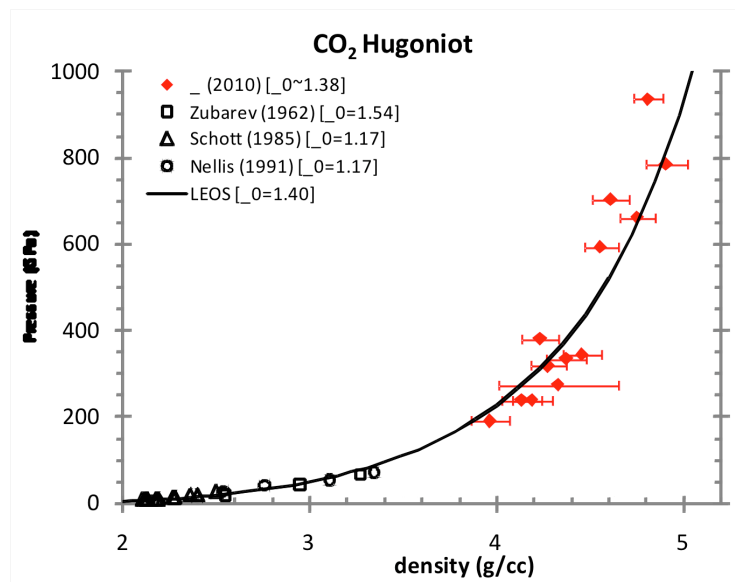


Figure 1 - Previous experimental measurements of the CO₂ Hugoniot (open markers) reached 80 GPa. In FY10, the OMEGA laser was used to extend the range to 200-950 GPa (filled diamonds). The CO₂ shock pressure and density were inferred by shock velocity measurements impedance matched to a quartz standard, using the Hicks (2005) quartz equation of state.

Melt and re-solidification in Tin

This was the first set of experiments investigating the use of velocimetry for exploring the melt line of tin. The strategy was to develop a drive to shock melt the tin and then ramp compress it across the liquid-solid phase boundary. While analysis of the data is ongoing, a number of important observations were made. We verified that the sample design was feasible, produced data across a wide range of shock pressures (20-200 GPa) and utilized a

reference material (Al) on each shot. Initial designs, based on extrapolation of diamond pressure-intensity measurements made at high pressures, proved to overestimate the achieved pressure. We were able to generate the necessary data by utilizing the calibrant. This data will serve as the basis for future designs. Lastly, we observed an interesting change in the reflectivity of the tin during the apparent release portion of the loading. This remains to be explained.

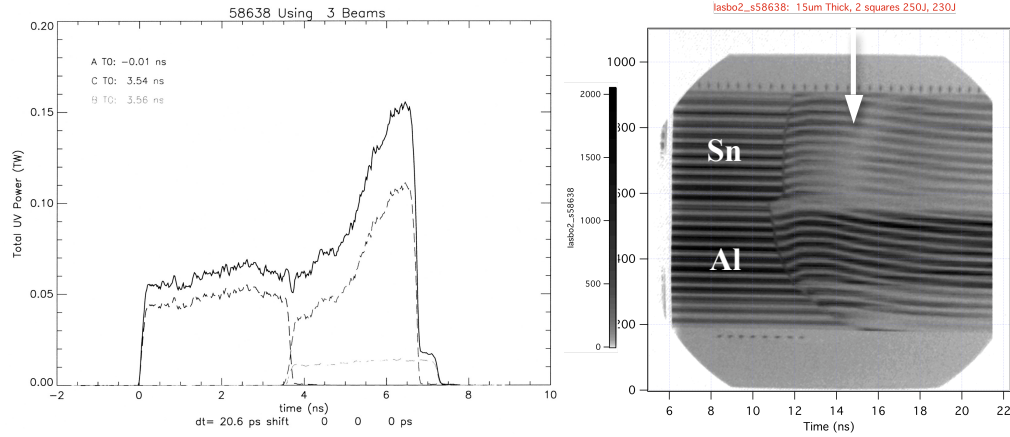


Figure 1 - Composite shock-ramp pulse shape (a) used to generate first attempt at compression driven resolidification in tin. Note late time reflectivity changes (arrow) that occur only in the tin.

II High-Temperature Plasma Opacity

Opacity experiments in FY10 had three main goals. The first addressed physics questions from the very successful 2009 Ti opacity shots, where the observed Ti continuum opacity didn't match code predictions, though spectral absorption lines from charge states consistent with ~ 120 eV LTE sample temperatures matched the code quite well. A modification in the configuration was made using thinner Ti samples, and new data were successfully taken on a half-day in January. A follow-up full-day experiment is scheduled for FY11.

The second goal was to better characterize the X-ray framing cameras (XRFCs) used on the experiments. NIF data from November 2009 revealed that the gain, and gain profile, of a microchannel plate detector strip was sensitive to the relative delays between individual strips, due to electromagnetic crosstalk in the pulser input lines and the detector strips themselves. This effect produced $\sim 3\times$ differences in gain between strips, $\sim 2\times$ changes in the relative point-to-point gain in a single strip (compared to a synchronized-strip baseline case), and 30-50% changes in gain from one edge of a strip to the other (transverse to the pulse propagation direction). The latter effect would impair the analysis of space-resolved gated absorption spectra if a similar effect occurred on the cameras used on opacity experiments. Data was taken for three framing cameras at Omega on July 8, measuring these effects as a function of interstrip delay and gated detector pulsewidth. While the XRFC data showed $\sim 2\times$ differences in gain between strips, and significant (50-100%) changes in point-to-point relative gain along a strip, no significant gain variation across the strip was measured. Thus the performance of the camera was not a factor in the discrepancy in the Ti data.

The third goal was to perform comparisons between short-pulse heated opacity measurements with similar long-pulse conditions (Ti, $T \approx 100$ -150 eV, density ~ 0.1 -1.0 g/cm³). In principle, much higher temperatures are possible with short pulse heated materials, but questions exist whether LTE conditions can be maintained. In these experiments, the EP sidelighter beam is operated at 250-800J, 100 ps pulsewidth and broad focus to heat an opacity sample at intensities between 10^{15} - 10^{17} W/cm². The EP backlighter beam is delayed by 100-500 ps and then operated at 800 J-1000 J, 10 ps to drive a broadband 3-6 keV backlighter. The backlighter x-rays probe the hot, expanded opacity sample. A separate line of sight allows space- and energy-resolved sample emission spectra to be taken in a different spectral

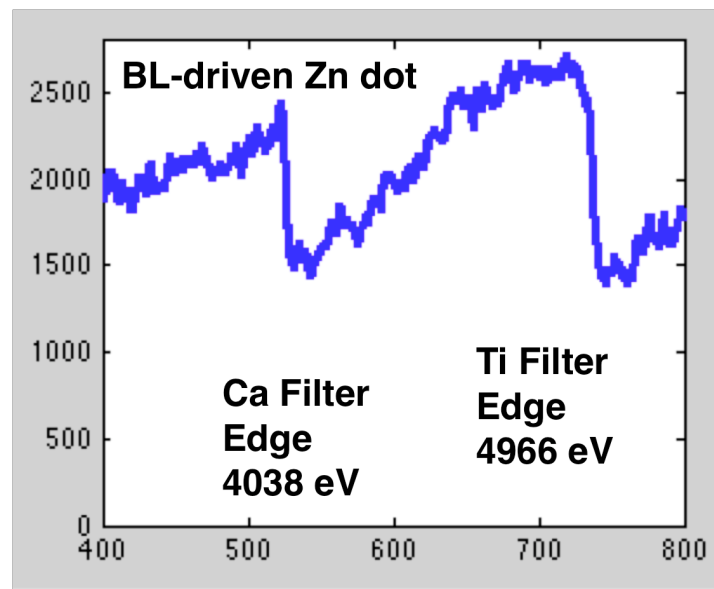


Figure 1 - Initial Zn microdot broadband backlighter spectra from ~ 3 to 6 keV photon energy.

band. The experiment uses the two opacity spectrometers which were transferred to Omega-EP from the 60 beam Omega chamber, and fielded with “rotating SPCA” frames and time-integrated image-plate detectors. Shots in February demonstrated an opacity-quality broadband backlighter using a Zn microdot on an Al substrate, with data shown in Figure 1. (Subsequent shots using a CH substrate failed due to very high instrument backgrounds, but may have reflected a change in the pointing or laser conditions.) Further optimization of the backlighter will take place in FY11. In parallel, space-resolved broadband emission spectra from 10-50Å were obtained from a CH/Ti/CH/Al exploding-foil sample (driven by the EP Sidelighter at $\sim 10^{16} - 10^{17}$ W/cm²). Al, C, and O line features have been identified from a shot at lower intensity, along with a broad continuum (see Figure 2). Bright Ti emission is seen at higher intensity. Absorption spectra from the Ti were not seen; FY11 shots will assess

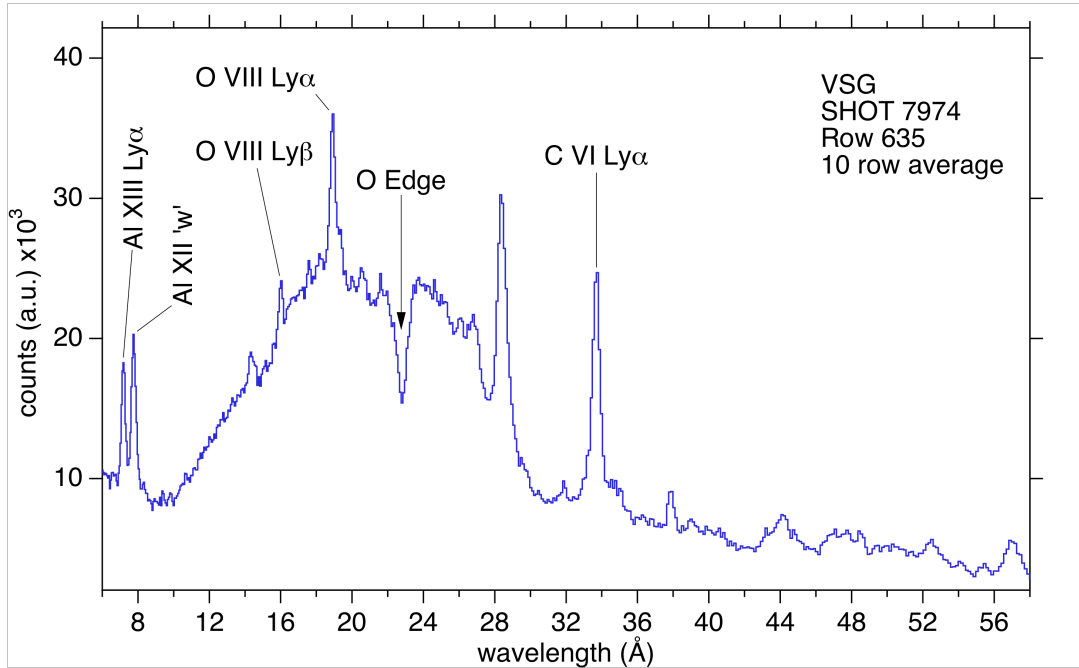


Figure 2 - X-ray Emission spectrum from the interior of the laser-driven CH/Ti/CH/Al foil, with initial line identifications.

whether this is due to cool Ti plasma conditions, or perhaps mistiming of the EP backlighter and sidelighter. The source of the O lines is being investigated.

III. Hydrodynamics

Kelvin-Helmholtz Instability Experiments

Kelvin-Helmholtz (KH) growth experiment was performed using a platform, successfully developed in earlier OMEGA experiments [1-3]. The main goal of the most recent campaign was a measurement of turbulent mixing on an interface between CRF foam and I-doped plastic. Figure 1 shows target schematic, which consists of a plastic ablator and a shock tube. In the shock tube the interface between low-density foam and high-density plastic had pre-

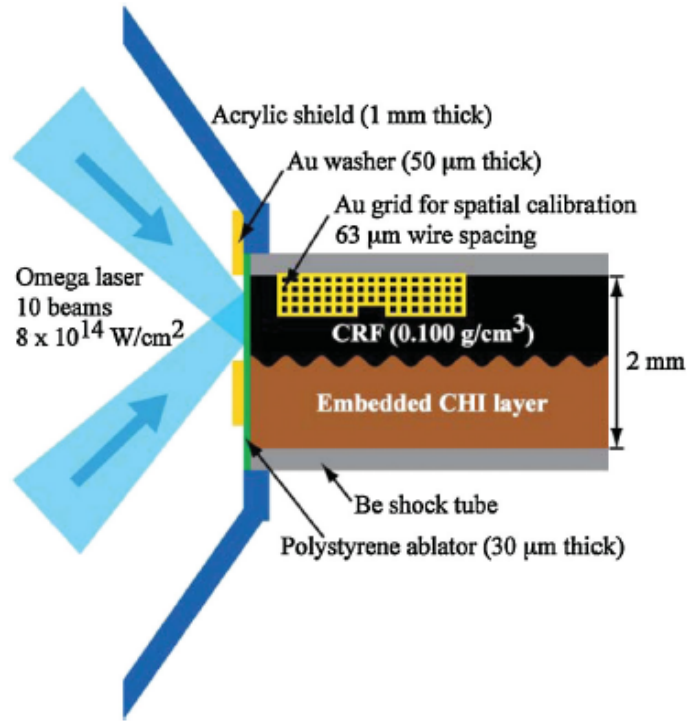


Figure 1 - Experimental configuration. The interface between lower density CRF foam and higher density I-doped plastic had a pre-imposed 2D modulation with wavelength of 400 μm . Three densities of CRF foam were used; 50, 100, and 200 mg/cm^3 .

imposed sinusoidal modulation at wavelength of 400 μm and amplitude of 30 μm . The central part of the plastic target contained a layer of I-doped CH to increase a contrast to 5 keV backscatterer x-rays. The ablator of the target was directly driven with laser light, producing strong shock that propagated through the target. The shock produced a velocity gradient at the interface between foam and plastic. This velocity difference between two materials resulted in the KH growth of the surface modulations. The density of foam was varied from 50 mg/cc to

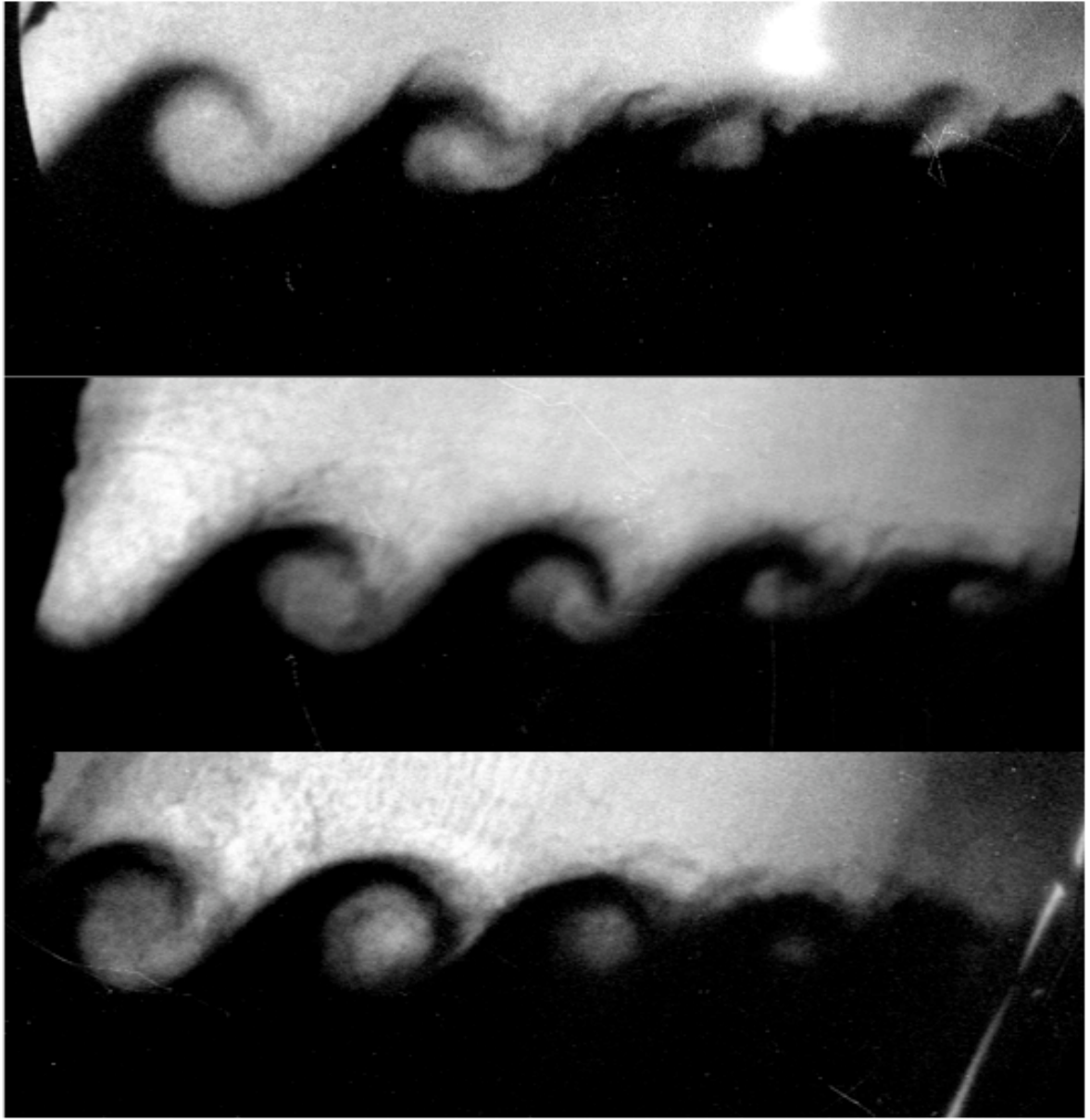


Figure 2 - X-ray radiographs of KH growth were taken with (a) 50 mg/cc CRF foam at 47 ns, (b) 100 mg/cc CRF foam at 75 ns, and (c) 200 mg/cc CRF foam at 117 ns. The vortices on right hand side of images experienced more KH growth than at left-hand side. Short-scale mix can be seen as “hairy-like” structures on top of vortices from pre-imposed modulations.

100 and 200 mg/cm³. Turbulent mixing between a foam and plastic materials was expected to grow from short-scale surface finish modulations (with rms amplitude of 100 nm) on the

interface between two materials.

Figure 2 shows experimental data. The shock travelled from left to right, so the modulations at the left part of the image had more time to grow than the modulations at the right part. The light color in the image corresponded to foam material, while dark color to plastic. The initial sinusoidal, 400- μm -wavelength modulation developed into the vortexes. In addition, the growth of short-scale modulations due to surface imperfections developed the “hair-like” non-uniformities. These non-uniformities represent turbulent mixing of two material, as expected since the Reynolds number was high in this experiment, $\text{Re} \sim 1\text{e}6$. The Reynolds numbers in hydrodynamic simulations, used to model the experiments, typically do not exceed $\sim 1\text{e}3$ due to finite spatial resolution of spatial grids. Therefore the simulations themselves are not expected to predict correctly evolution of short-scale mix. These experimental data are used to develop and validate mix models that are based on post-processing of hydrodynamic simulations, currently in progress.

References:

1. O. A. Hurricane, High Energy Density Phys. **4**, 97 (2008).
2. E. C. Harding *et al.*, Phys. Rev. Lett. **103**, 045005 (2009).
3. O. A. Hurricane *et al.*, Phys. Plasmas **16**, 056305 (2009).

High mach-number Cu-foam Jet Experiments

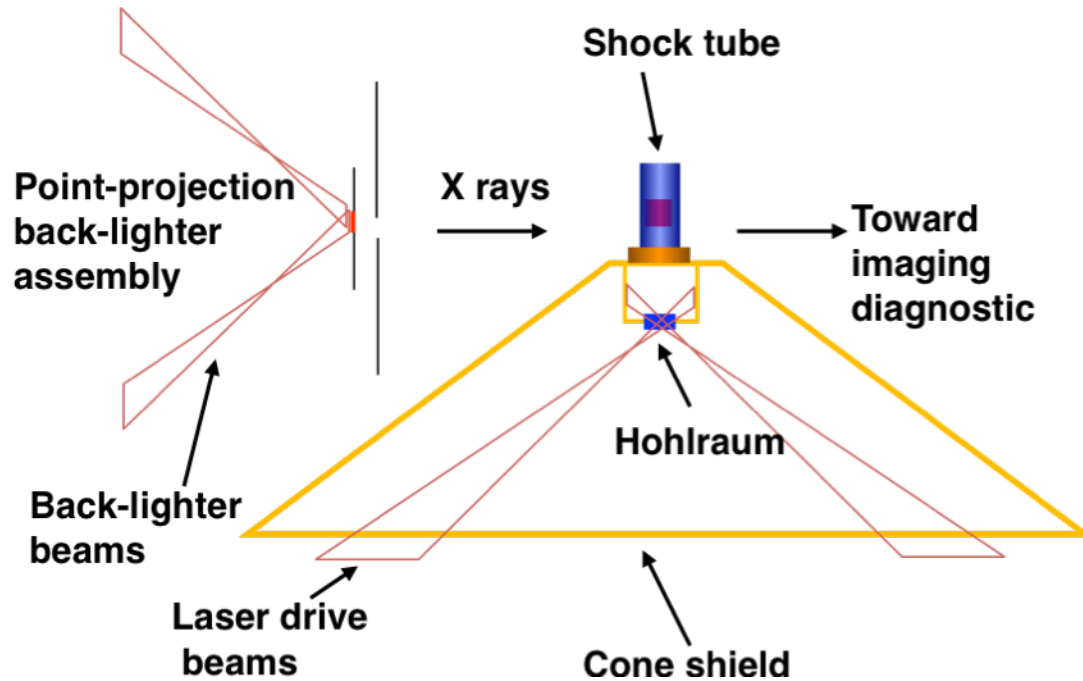


Figure 1 - Experimental configuration. The jet is generated in a shock tube, driven by a hohlraum x-rays. X-rays, generated by a point-projection back-lighter, radiograph the jet at various times, from 15 to 35 ns after the beginning of the drive.

Some of the most challenging experiments to model for hydrodynamics codes are jet-evolution experiments. Several aspects of hydrodynamics-code predictions can be validated by these experiments, including physics of shocks, material flows, and equation of state physics. The current experiment studied evolution of a Cu-foam jet into a low-density plastic foam. Figure 1 shows the experimental set-up. A high-Mach number jet is generated in a shock tube, driven by x-rays from a hohlraum irradiated with 12 OMEGA drive beams. A point-projection backlighter x-ray source, driven by 3 beams, generated ~ 4.3 keV x-rays which illuminate the jet at time intervals ranging from 15 to 35 ns after the beginning of the drive. The cone shield prevents x-rays generated in the hohlraum, from reaching the imaging diagnostic, which would contribute to background on the data.

Figure 2 shows an example of a radiograph taken at 30 ns of the jet. In the image, a mushroom-like jet of Cu-foam material (darker color) penetrates the plastic foam (lighter color). The height, width, and position of the jet with respect to the grid (shown on the right side of the image) are some of the measures used to compare with code predictions. In addition, the shock position and compression of the plastic foam will also be used to test various aspects of hydrodynamics codes. Preliminary simulations of jet evolution and shock

propagation are close to experimental data, with much better agreement than in previous campaigns, primarily due to well-made Cu foams.



Figure 2 - X-ray radiograph of a Cu-foam jet driven into a plastic foam with density of 0.1 g/cc. The image is taken at ~ 30 ns after the beginning of the drive. The jet structure is clearly visible. The height, width, and position of the jet as well as the shock position and compression of the plastic foam will be used to test various aspects of hydro-codes.

IV. X-Ray Source Development and Application

Bright, tunable x-ray sources are necessary for radiography applications, radiation-effects experiments and as backlighters for high-energy-density experiments. LLNL's x-ray source development campaign had one full day and two half days of shots (22 shots total) during which two types of a multi-keV -ray source were shot. These experiments were performed in

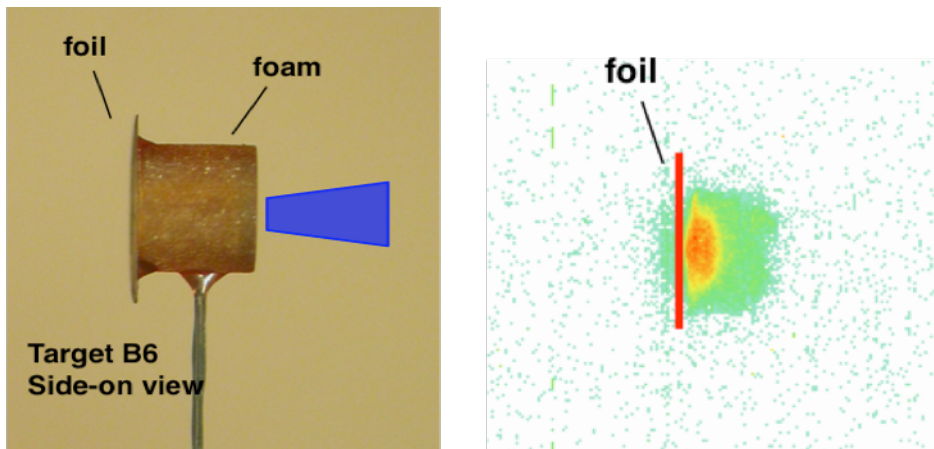


Figure 1 - (left) a hybrid foam-foil target that was shot in the LLNL-CEA x-ray source development experiments. Five or six OMEGA laser beams entered the target's foam cylinder from the left and created x-rays from the Ti foil at the right. (right) A x-ray framing camera image from shot 56933 of a hybrid foam-foil target (foam 2 mg/cm^3 , $3 \mu\text{m}$ thick foil).

collaboration with French scientists from the CEA. Two half days (XRSD-10A, XRSD-10C) were investigated the performance of titanium foil targets confined by cylinders of ultra-low-density SiO₂ aerogel material. A photo of one of the targets is shown on the left in Figure 1 (with bundled laser beams shown schematically), and a -ray image of the Ti K-shell emission (energies > 4.5 keV) from the target in shot 56933 is shown on the right in Fig. 1. Target yields were studied as a function of the aerogel density, the aerogel volume, the foil thickness, the laser intensity, and the laser pulse length. Data is consistent with CEA predictions of an optimal aerogel density for maximal Ti K-shell radiation production.

Dedicated investigations of x-ray emission from noble gases were also carried out (XRSD-10B, XRSD-10C). During these experiments, the scaling of x-ray yield from gas-filled beryllium cans was studied as a function of gas fill pressure and gas mixture. Pure Ar, Kr and

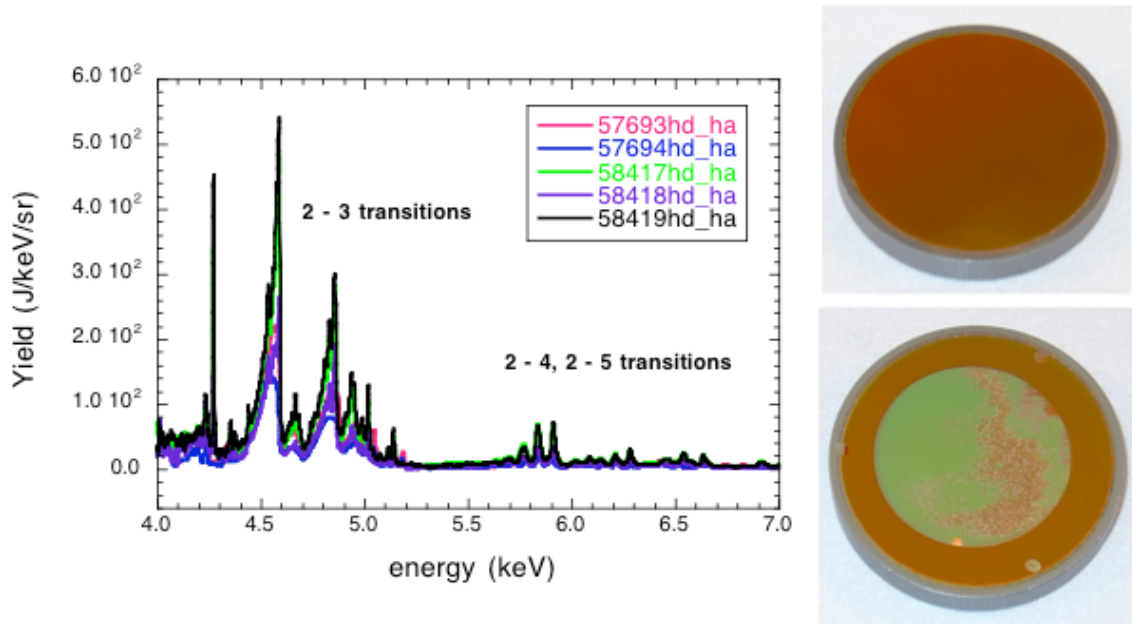


Figure 2 - (left) The measured spectra from a series of Xe-filled targets shot during the x-ray source development and application campaigns in FY2010. The x-rays from the targets were used to study the response of radiation-hardened by design mirrors and photovoltaic solar cells. (right) Before and after images of a mirror specimen that was exposed to the unfiltered output of an Ar gas target on shot 57692.

Xe targets were shot, as were mixed Ar:Xe targets, for all targets, fill pressures ranged from 1.0 to 1.5 atm. Figure 2 shows the measured spectra from five Xe-filled targets shot on the two dedicated days. During the XRSD-10B series of shots, the x-ray environments produced by the targets were also applied to investigate changes in the material properties of, and surface interactions on sets of samples in response to x-ray loading. Samples included radiation-hardened by design mirrors and photovoltaic solar cells. An example of one specimen is shown in Fig. 2. Changes in reflectivity and surface profiles of the mirrors, and changes in the performance of the solar cells were characterized for exposures of several different fluences and spectral contents, which greatly expands our knowledge of the x-ray survivability of these materials.

V. Diagnostic technique development

Development of VISAR with a target-mounted turning mirror

It is known that measurement of the shock speed inside a quartz (Qz) window is a reliable way to understand the hohlraum drives [1]. One of the NIF experiments (Rad-Transport) will apply this technique to characterize the drive inside a half-hohlraum. Because the VISAR located along the equator on NIF, characterization of the drive at the end of a half-hohlraum requires the use of a target mounted turning mirror. A potential failure mode was loss of

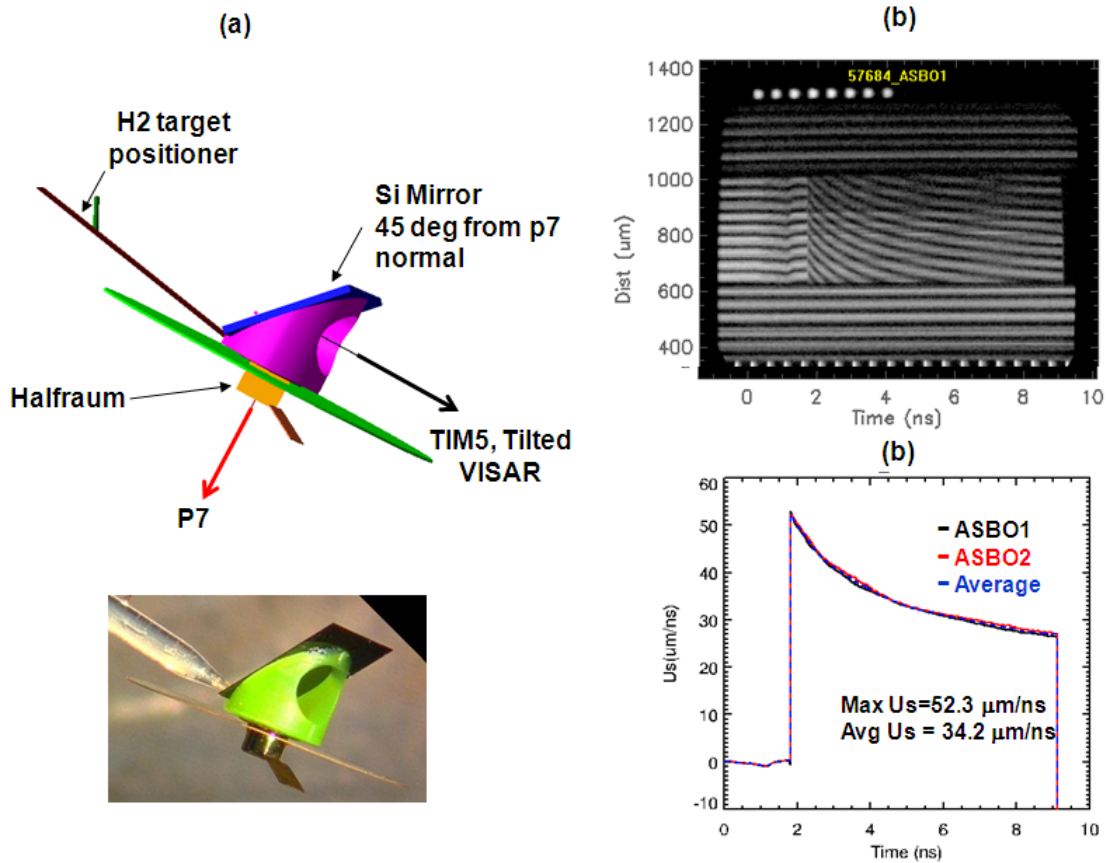


Figure 1 - (a) VISAR mirror test experimental configuration. (b) An example of VISAR data measuring the shock speed in a quartz window. No blanking is observed. (c) The measured shock speed is 52 $\mu\text{m/ns}$, corresponding to a ~ 50 Mbar ablation pressure.

reflectivity from the turning due to M-band x-ray preheat. An experiment was designed to empirically test the turning mirror performance under an equivalent heat loading of the NIF

Radiation Transport experiment. We designed a new configuration that carefully followed constraints from the simulations and experiments, as shown in Figure 1 (a). We tested 2 types of mirrors: Si and nano-Diamond mirrors. The experiments were highly successful: no mirror blanking was observed. One example of VISAR image is shown in Figure 1 (c). From this data we measured the peak shock velocity up to 50 km/s, or ~ 50 Mbar pressure in quartz. This is the highest-pressure shock measured inside quartz to date. Both mirror types worked well and delivered high-quality meaningful data. From this data, it is expected that the mirrors will survive until the thinnest ablator section burns through and that the NIF experiment will deliver meaningful measurements.

[1] R. E. Olson et al., RSI, 77, 10E523 (2006).

Beryllium X-Ray Thomson Scattering

The objective of the BeXRTS-10 campaign was to heat isochorically beryllium utilizing short-pulse-generated hot electrons, and measure the plasma temperature by means of non-collective x-ray Thomson scattering with high time resolution. We employ the two Omega EP short-pulse beams with the backlighter beam heating a 250 μm beryllium cube and the sidelighter beam creating a Zn K-alpha x-ray probe at 8.6 keV. On this shot day, the sidelighter was delayed by 200 ps with an accuracy of ~ 25 ps as observed by an ultra-fast x-ray streak camera.

Zinc K-alpha x-rays are scattered off the Be and collected by the Zinc von Hamos (ZVH) spectrometer, that uses a curved, highly efficient HOPG Bragg-crystal for energy dispersion and focusing in the non-dispersive direction. The spectrometer, specifically developed for the K-alpha scattering project, had to be rebuilt to meet the new safety standards, and the new instrument was successfully fielded on this shot day.

We had a total of 6 shots including 2 low energy activation shots. The latter ones were used to measure a high-resolution source spectrum and to record background signal levels. The facility made a big effort to establish the beam timing, i.e. the delay between the backlighter and the sidelighter beams, on previous shot days. We successfully used the single photon counting camera (SPC) to observe the Zn K-shell source spectrum.

Compared to a previous shot campaign, we significantly reduced the target size and used lower-Z shields aimed at reducing Bremsstrahlung levels. We also tested different shield compositions. At the end of the day we successfully recorded an inelastically scattered Compton signal from isochorically heated Be (cf. Fig. 1), employing 62 J in the backlighter beam and 250 J in the sidelighter beam, which is significant progress compared to the previous shot campaign.

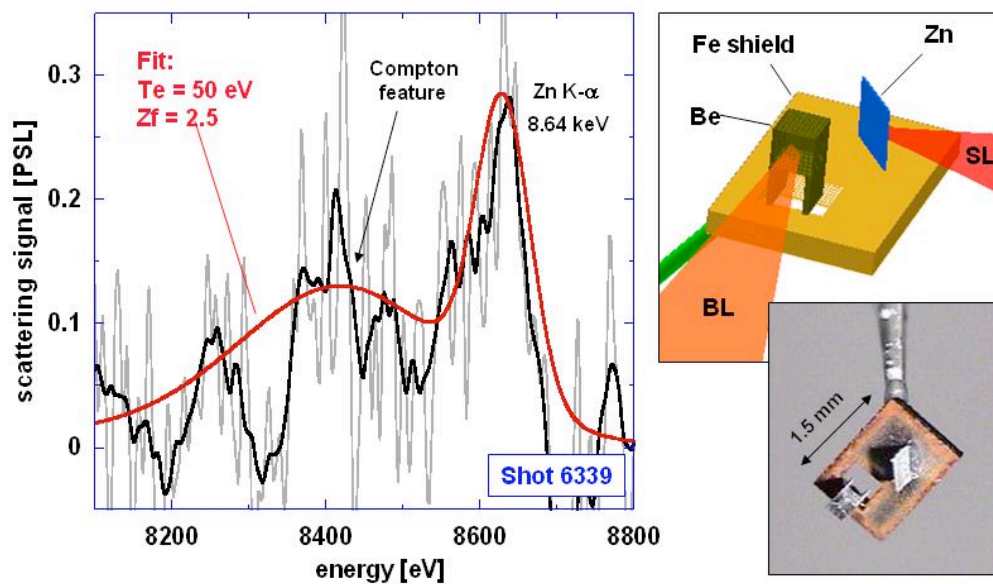


Figure 1 - Experimental configuration (right) and x-ray Thomson scattering spectrum (left) from isochorically heated Be, utilizing a Zn K α source line at 8.6 keV. The experimental data are fitted with $T_e = 50$ eV and ionization of $Z_f = 2.5$.

High-Energy Backlighter Development

The goal of this experiment was to compare the backlighter conversion efficiencies of high-Z materials driven by short pulse and long pulse lasers. Short pulse generated x-rays are believed to result from hot electrons that collide with K-shell electrons, causing K- α x-ray fluorescence. Long pulse generated x-rays are believed to be created by thermal heating and ionization of the material. Our goal was to perform systematic comparisons at high x-ray energies. The Omega-EP laser system is ideal to do this type of test, since both short pulse and the long pulse lasers are available to illuminate a target using the same diagnostics. In this set of experiments, we tested 3 different types of materials: Cu, Ag, and Sm. Our initial analysis shows the long pulse is much more efficient at generating the 8 keV Cu backlighter; whereas the 40 keV Sm x-ray is much more efficiently generated with the short pulse lasers. From these data, we observed that the conversion efficiencies are about the same at ~ 17 keV, driven by either long pulse or short pulse lasers. At 8 keV the long pulse laser was more efficient by a factor of 10, whereas at 22 keV, the short pulse laser was more efficient by a factor of 5.

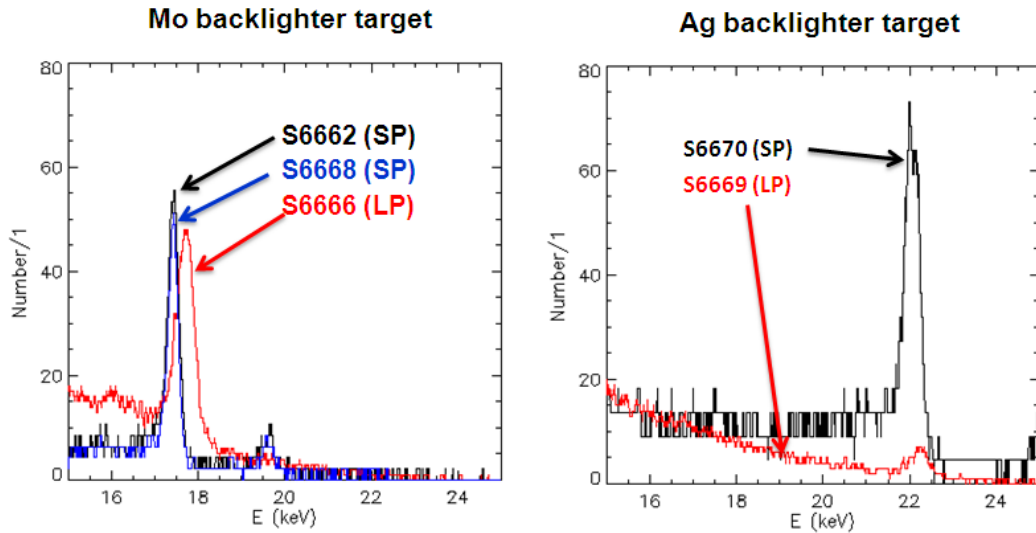


Figure 1 - Comparison of high-energy backlighter yields driven by the 1-ns $3-\omega$ long pulse (LP) laser versus the 100-ps $1-\omega$ short pulse (SP) laser. The data are taken with the single photon counting camera. When normalized by the laser energies, we find that the Mo backlighter conversion efficiencies are about the same either driven by the short pulse or the long pulse.

Broadband x-ray Laue diffraction development

The Lattice Scattering campaign uses the broadband thermal x-ray emission from a direct drive implosion capsule to perform single shot in-situ white light x-ray diffraction. This employs the classic Laue diffraction on a sub-nanosecond timescale to investigate material behavior during shock or ramp compression. This technique will give insight into the material microstructure as lattice defects will cause non-uniform strain in the atomic structure causing the diffraction spots to broaden and change shape. A directly driven implosion on the Omega laser is ideally suited for this technique providing a short burst (~ 150 ps) of bright broadband x-rays. We pointed the lasers to five different pointing locations on the capsule to maintain implosion symmetry. Figure 1 shows gated framing camera images of the implosion capsule on a previous campaign that had 42 beams for the implosion, while Fig 2. shows the improved symmetry by using the five different targeting locations. In principle symmetry can be improved even further by adding more locations.

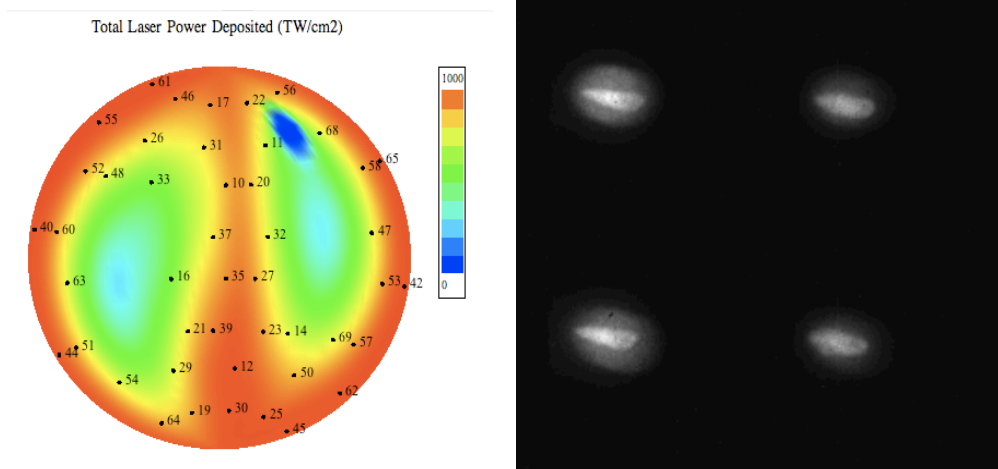


Figure 1 - The Total Laser power deposited and gated framing camera images from the implosion capsule using 42 beams pointed to the center of the capsule.

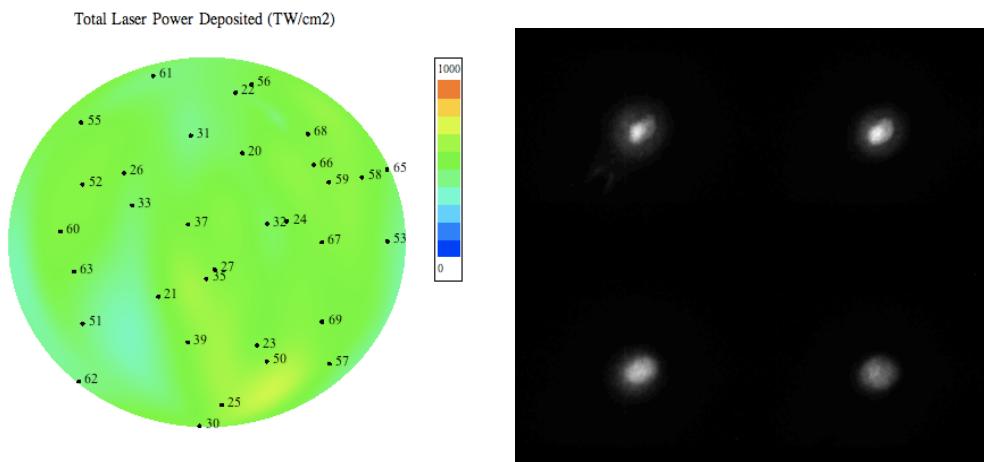


Figure 2 - The Total Laser power deposited and gated framing camera images from the implosion capsule using 33 beams 5 different targeting locations on the capsule

For these experiments we designed and qualified the Broad Band X-Ray Diffraction (BBXRD) diagnostic Figure 3. The diagnostic is designed with a tapered profile to allow as many beams as possible to reach an implosion capsule placed 20 mm away from the single crystal target which sits on the front plate of the BBXRD. The inside of the BBXRD has four trapezoidal image plate detectors on the tapered sides and a square piece on the back to record the transmitted diffraction. The back plate has a hole to allow simultaneous VISAR measurements to be made from the rear surface. We successfully demonstrated the diagnostics capability on two campaigns of shock-compressed silicon, shown in Fig. 4, and copper. For the silicon images shown we can estimate the anisotropy in the compression by the shift in the spots to be about 8% along the driven direction.

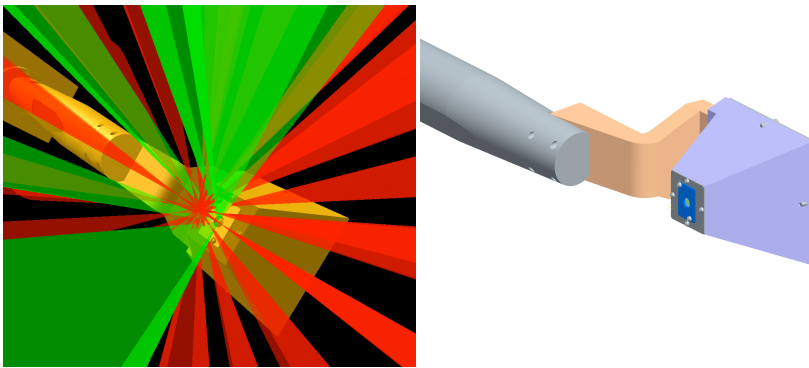


Figure 3 - The BBXRD diagnostic in the VISRAD model showing the location of the implosion capsule and beams and CAD model.

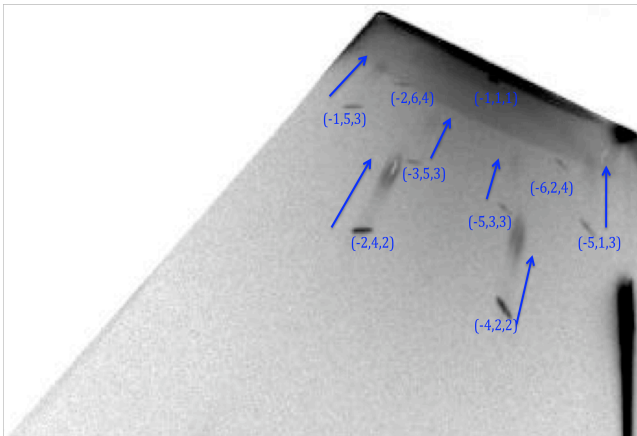


Figure 4 - The tip of one of the trapezoidal image plates showing diffraction from uncompressed and shock compressed silicon.

Powder X-ray diffraction development

The objective of this campaign is to demonstrate the use of powder x-ray diffraction methods in the characterization of dynamically loaded (shocked and ramped) polycrystalline materials, particularly with a view to application on forthcoming NIF experiments. Such x-ray diffraction methods offer insight into processes occurring on the scale of the material lattice, which in turn determine the macroscopic response of the material to dynamic loads (e.g. its strength).

To date the campaign has demonstrated x-ray diffraction from polycrystalline tantalum foils using a quasi-monochromatic molybdenum backlighter source (see figure below). Future

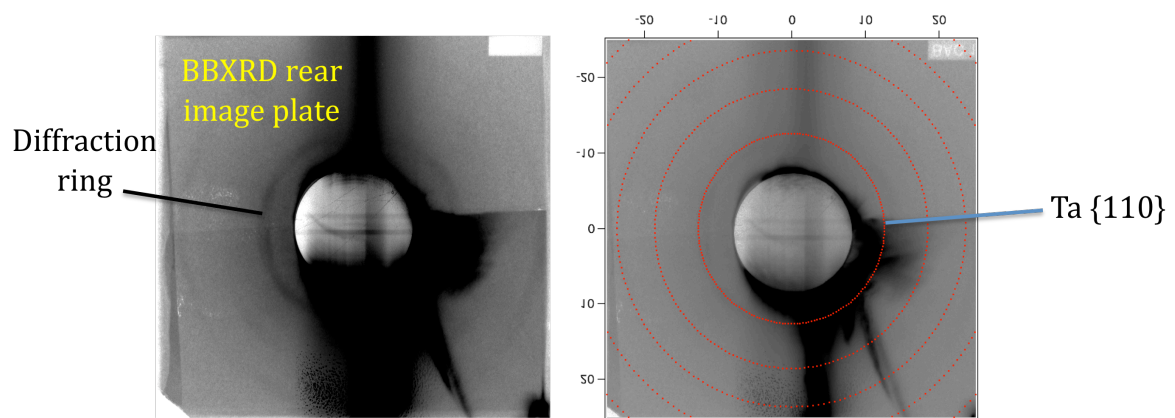


Figure 1 - Diffraction signature from polycrystalline tantalum foil using 17.5keV x-ray source and LLNL Broadband X-ray Diffraction (BBXRD) diagnostic. Each crystallographic plane (hkl) generates a characteristic cone of x-rays; intersection of these cones with the image plate detectors result in characteristic ring pattern. Right: calculated pattern shown overlaid over data.

campaigns will concentrate on improving the signal-to-noise in the diffraction signal, and will then aim to utilize this signal to characterize tantalum under a variety of shock and ramp-loaded conditions.

Powder x-ray diffraction measurements of solid Fe, Sn, and Ta to 500 GPa

An experimental platform has been developed to measure powder x-ray diffraction on solid samples at pressures above Hugoniot melt. Fe, Sn, and Ta samples were sandwiched between a diamond pusher and window, and ramp-compressed to high pressure and density using up to 6 OMEGA beams. VISAR velocity measurements were used to infer the pressure history in the sample, and the 8.37 keV Cu-He α x-ray source, driven by 10 beams, was timed to coincide with the peak pressure. The diffraction signal is collimated through a 300- μ m-diameter aperture in a 150- μ m thick Ta substrate, and captured on image plate detectors. Density is inferred from the diffraction data by assuming a crystal structure, then verifying self-consistency with a best fit to density. Maximum diffraction pressures attained on Fe, Ta, and Sn samples were 480, 310, and 220 GPa, respectively, all above Hugoniot melt. Data from iron samples are shown in Figure 1.

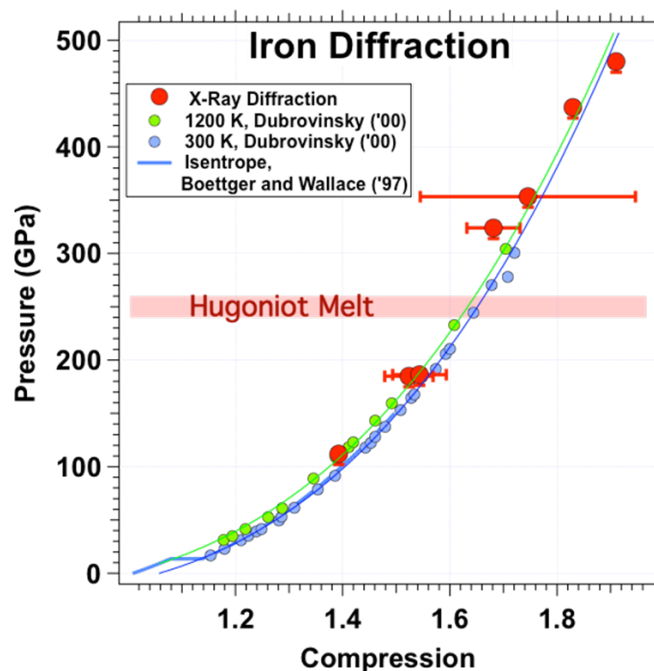


Figure 1 - In FY2010, the OMEGA laser was used to obtain x-ray diffraction measurements of solid iron (red circles) at pressures above the Hugoniot melt (red band at 250 GPa). The results are consistent with Fe remaining in a HCP structure up to the highest pressures observed (~480 GPa). Diffraction data from diamond anvil cells (Dubrovinsky 2000) are also shown, along with a theoretical isentrope from Boettger and Wallace (1997).